Available online at www.sciencedirect.com
ScienceDirect
Comput. Methods Appl. Mech. Engrg. 344 (2019) 998–1020
Computer methods in applied mechanics and engineering
www.elsevier.com/locate/cma

A divergence free weak virtual element method for the Stokes–Darcy problem on general meshes☆

Gang Wang[a], Feng Wang[b], Long Chen[c,d,*], Yinnian He[a]

[a] School of Mathematics and Statistics, Xi'an Jiaotong University, Xi'an, Shaanxi 710049, PR China
[b] Jiangsu Key Laboratory for NSLSCS, School of Mathematical Sciences, Nanjing Normal University, Nanjing 210023, PR China
[c] Department of Mathematics, University of California at Irvine, Irvine, CA 92697, USA
[d] Beijing Institute for Scientific and Engineering Computing, Beijing University of Technology, Beijing 100124, PR China

Received 17 March 2018; received in revised form 5 September 2018; accepted 12 October 2018
Available online 30 October 2018

Abstract

This paper presents a weak virtual element method on general meshes for the Stokes–Darcy problem with the Beavers–Joseph–Saffman interface condition. The velocity is discretized by the $\boldsymbol{H}(\mathrm{div})$ virtual element. The pressure is approximated by discontinuous piecewise polynomials. Besides, a polynomial space on the element faces is introduced to approximate the tangential trace of the velocity in the Stokes equations. The velocity on the discrete level is exactly divergence free and thus the exact mass conservation is preserved in the discretization. The well-posedness of the discrete problem is proved and an a priori error estimate is derived that implies the error for the velocity in a suitable norm does not depend on the pressure. A series of numerical experiments are reported to illustrate the performance of the method.

Keywords: Stokes–Darcy problem; Beavers–Joseph–Saffman condition; Divergence free; Pressure-robustness; General meshes

1. Introduction

Coupling incompressible flow and porous media flow has received increasing attention over the past decades, being involved in many applications, such as ground water contamination and industrial filtration. This coupled phenomenon is mathematically expressed by the Stokes–Darcy problem that consists of the Stokes equations to govern the flow in

☆ The work of Gang Wang and Yinnian He was supported by the Major Research and Development Program of China Grant No. 2016YFB0200901 and National Natural Science Foundation of China Grant No. 11771348. The work of Gang Wang was supported by 2016 China Scholarship Council (CSC No. 201606280158). F. Wang was supported by National Natural Science Foundation of China (Grant Nos. 11871272, 11871281. L. Chen was supported by the National Science Foundation (NSF) DMS-1418934, by National Natural Science Foundation of China (Grant No. 11671159), and in part by the Sea Poly Project of Beijing Overseas Talents.

* Corresponding author at: Department of Mathematics, University of California at Irvine, Irvine, CA 92697, USA.
E-mail addresses: anda20082012@stu.xjtu.edu.cn (G. Wang), fengwang@live.cn (F. Wang), chenlong@math.uci.edu (L. Chen), heyn@mail.xjtu.edu.cn (Y. He).

https://doi.org/10.1016/j.cma.2018.10.022
0045-7825/

the free fluid region and Darcy's law to describe the flow in the porous media, and three transmission conditions at the interface, namely mass conservation, the balance of the normal stresses and the well-known Beavers–Joseph–Saffman condition [1,2].

Various numerical methods have been developed to approximate the solution of the Stokes–Darcy problem (see for instance [3–11]), most of which are based on the second order primal formulation of Darcy's law. The numerical schemes in these references do not satisfy the exact mass conservation property. In this paper, we adopt the perspective of the mixed form in which both the velocity and the pressure simultaneously arise in Darcy's law. So that two variables in the whole domain, i.e., the velocity and the pressure, are now needed to be well approximated. It is emphasized that the velocity field on the discrete level must retain normal continuity and preserve the exact mass conservation property that is critical for the transport problem to avoid creating artificial mass sources and sinks [12]. Therefore, the mixed finite element method (MFEM) [13] is a better choice for dealing with this problem.

There are several stable and convergent mixed finite element discretization strategies developed for the Stokes–Darcy problem. In [14], the authors studied the mathematical theory and associated numerical analysis of a mixed variational formulation. There, standard Stokes elements like the Taylor–Hood element were proposed for the Stokes equations, and mixed finite element like the Raviart–Thomas element for Darcy's law. They also introduced a Lagrange multiplier representing the trace of the Darcy pressure on the common interface to enforce the continuity of the normal velocity weakly. A similar method was also presented in [15–17], where the Bernardi–Raugel element was employed for the Stokes equations. To prevent one from using Lagrange multipliers and impose the first type of transmission conditions essentially, the authors in [18,19] used divergence conforming finite elements for the velocities in the whole domain via the ideas of discontinuous Galerkin (DG) method [20]. One advantage of such an approach is that the velocity on the discrete level satisfies the exact divergence free constraint. The other is that there only exists an integral term of the tangential velocity in the bilinear form. More research concerning MFEM for the Stokes–Darcy problem can be found in [21–24]. It should be mentioned that all of these methods are proposed on simplicial meshes.

In the recent years, several novel numerical methods on general meshes have been introduced, and then received attention in partial differential equations since their great flexibility of element-geometry. Such methods include virtual element method (VEM) [25–29], weak Galerkin (WG) method [30–32], mimetic finite difference (MFD) method [33–35], hybrid high order method [36,37], hybridizable discontinuous Galerkin (HDG) method [38–40], and so on. Within our knowledge, however, there are few studies of the Stokes–Darcy problem by using these methods. A family of WG finite element discretization has been proposed in [41] where the velocity and the pressure are approximated by discontinuous piecewise polynomials, respectively, and weak gradient and divergence are introduced to handle the nonconformity. DG method for the Stokes equations combining with MFD method for Darcy's law was studied by Lipnikov et al. in [42]. In these works, the error estimates for the velocity still depend on the pressure. Recently, a strongly conservative HDG/mixed finite element method for the Stokes–Darcy problem has been presented in [43]. In that work, the HDG method and the MFEM were used in the Stokes and Darcy subdomains, respectively. The stability of the numerical scheme holds if the penalty parameter is sufficiently large. The use of MFEM in the Darcy subdomain also limits the application of the method to simplicial meshes.

The focus of this paper is to apply a new numerical method proposed in [44] for the Stokes equations to the Stokes–Darcy problem by employing an exact divergence free element on polygonal or polyhedral meshes. For the Stokes equations, Chen and Wang [44] proposed a divergence free weak virtual element method (WVEM) on general meshes. They used $\boldsymbol{H}(\mathrm{div})$ virtual element [45,46] to discretize the velocity, and discontinuous piecewise polynomials to approximate the pressure. In addition, the tangential continuity is enforced by introducing a polynomial space on the element faces and defining a weak symmetric gradient following the idea of WG method [30]. The WVEM is exactly divergence free and robust with respect to the pressure.

As an extension, we shall combine the WVEM for the Stokes equations and the $\boldsymbol{H}(\mathrm{div})$ virtual element for the Darcy law to end up with a stable discretization for the coupled problem. We point out that two issues need to be addressed. First, we aim to choose a discrete space for Darcy's law such that the interface condition of mass conservation becomes essential. Here we will use $\boldsymbol{H}(\mathrm{div})$ virtual element to approximate the velocity in Darcy's law, which leads to a unified discretization for both the Stokes and Darcy sides. Consequently, the velocity on the discrete level still belongs to the exactly divergence free space, and the tangential space on the element faces is only defined in the Stokes domain. This choice also allows the use of hanging nodes on the interface in the implementation. Second, as mentioned before, the bilinear form involves an integral term of the tangential velocity. We define a suitable $\boldsymbol{H}^1$ seminorm $|||\cdot|||$ such that the

discrete scheme is stable and an a priori error estimate can be derived. To this end, a mesh dependent $\boldsymbol{H}^1$ seminorm on the discrete space is defined in (4.2), and the well-posedness of the discrete scheme is proved by using the classical saddle point theory. We therefore present an approach that is exactly divergence free and pressure-robust.

Specifically, let $\boldsymbol{u}$ and p be the velocity and the pressure of the Stokes–Darcy problem, respectively, and assume that $(\boldsymbol{u}_h, p_h)$ is the solution of the discrete problem (4.1) and $(\boldsymbol{u}_I, p_I)$ is the interpolation of the exact solution, then we obtain

$$|||\boldsymbol{u}_h - \boldsymbol{u}_I||| + \|p_h - p_I\| \lesssim h^k \left(\nu^{\frac{1}{2}} \|\boldsymbol{u}\|_{k+1,\Omega_s} + \mathbb{K}^{-\frac{1}{2}} \|\boldsymbol{u}\|_{k,\Omega_d} \right) + \nu^{-\frac{1}{2}} h \|\boldsymbol{f} - \boldsymbol{\Pi}_h^o \boldsymbol{f}\|_{\Omega_s},$$

where ν denotes the viscosity constant, $\mathbb{K}$ stands for the permeability, $\boldsymbol{f}$ is an external force and $\boldsymbol{\Pi}_h^o$ represents the piecewise $\boldsymbol{L}^2$ projection to $\boldsymbol{P}_k$ polynomial space.

Another point we would like to emphasize is that, unlike the traditional finite element methods, there are non-polynomial functions in the virtual element space. In other words, one does not know explicitly the shape function. The degrees of freedom are only used in the assembly process of the matrix. Thus the VEM is convenient to implement, especially for the vector space, e.g., $\boldsymbol{H}(\mathrm{div})$ virtual element space.

The paper is structured as follows. In Section 2, we shall recall and state the Stokes–Darcy model problem. In Section 3, the weak virtual element space will be introduced. The Stokes–Darcy problem is then discretized by the weak virtual element method in Section 4, where we also prove the well-posedness of the discrete problem. In Section 5, we derive an a priori error estimate in a suitable norm. In Section 6, numerical experiments are presented to validate the theoretical results. Finally, conclusions are drawn in Section 7.

2. Model statement

Throughout the paper, we often use bold fonts to express vector variables, operators, and spaces. Standard notations are defined for the scalar Sobolev space $H^s(D)$ or the vector Sobolev space $\boldsymbol{H}^s(D)$ $(s \geq 0)$ in an open bounded domain $D \subset \mathbb{R}^d$ ($d = 2$ or 3), equipped with norm $\|\cdot\|_{s,D}$ and seminorm $|\cdot|_{s,D}$. The space $H^0(D)$ (or $\boldsymbol{H}^0(D)$) coincides with $L^2(D)$ (or $\boldsymbol{L}^2(D)$), for which the norm and the inner product are represented by $\|\cdot\|_D$ and $(\cdot,\cdot)_D$, respectively. We also define the following vector Sobolev spaces,

$$\begin{aligned}
\boldsymbol{H}(\mathrm{div}, D) &:= \{\boldsymbol{v} \in \boldsymbol{L}^2(D) : \mathrm{div}\, \boldsymbol{v} \in L^2(D)\} \quad d = 2 \text{ or } 3,\\
\boldsymbol{H}(\mathrm{rot}, D) &:= \{\boldsymbol{v} \in \boldsymbol{L}^2(D) : \mathrm{rot}\, \boldsymbol{v} \in L^2(D)\} \quad d = 2,\\
\boldsymbol{H}(\mathbf{curl}, D) &:= \{\boldsymbol{v} \in \boldsymbol{L}^2(D) : \mathbf{curl}\, \boldsymbol{v} \in \boldsymbol{L}^2(D)\} \quad d = 3,
\end{aligned}$$

where the operators div and **curl** denote the standard divergence and curl. For any $\boldsymbol{v} = (v_1, v_2)$ in $\boldsymbol{L}^2(D)$, we will set $\mathrm{rot}\, \boldsymbol{v} = \frac{\partial v_2}{\partial x} - \frac{\partial v_1}{\partial y}$.

We consider a coupled Stokes–Darcy model in an open, bounded and convex polygonal or polyhedral domain $\Omega \subset \mathbb{R}^d$, consisting of a free fluid region Ω_s and a porous medium region Ω_d, with interface $\Gamma = \overline{\Omega}_s \cap \overline{\Omega}_d$, as depicted in Fig. 1. Denote by $\Gamma_s = \partial\Omega_s \setminus \Gamma$, $\Gamma_d = \partial\Omega_d \setminus \Gamma$ the outer boundary, thus we can express that $\partial\Omega = \Gamma_s \cup \Gamma_d$ and $\Gamma_s \cap \Gamma_d = \emptyset$. We also use $\boldsymbol{n}_s$ and $\boldsymbol{n}_d$ to denote the unit outward normal vectors on $\partial\Omega_s$ and $\partial\Omega_d$, respectively. Note that $\boldsymbol{n}_s = -\boldsymbol{n}_d$ on Γ.

Denote by $\boldsymbol{u} = (\boldsymbol{u}_s, \boldsymbol{u}_d)$ the fluid velocity and by $p = (p_s, p_d)$ the fluid pressure, where $\boldsymbol{u}_i = \boldsymbol{u}|_{\Omega_i}$ and $p_i = p|_{\Omega_i}$, $i = \{s, d\}$. In Ω_s, the fluid flow is assumed to be governed by the Stokes equations:

$$-\mathrm{div}(2\nu\epsilon(\boldsymbol{u}_s)) + \nabla p_s = \boldsymbol{f} \quad \text{in } \Omega_s, \tag{2.1a}$$

$$\mathrm{div}\, \boldsymbol{u}_s = 0 \quad \text{in } \Omega_s, \tag{2.1b}$$

$$\boldsymbol{u}_s = \boldsymbol{0} \quad \text{on } \Gamma_s, \tag{2.1c}$$

where $\nu > 0$ stands for the constant viscosity, $\epsilon(\boldsymbol{u}_s) = (\nabla \boldsymbol{u}_s + \nabla \boldsymbol{u}_s^T)/2$ is the symmetric gradient of $\boldsymbol{u}_s$, and $\boldsymbol{f} \in \boldsymbol{L}^2(\Omega_s)$ is a given external force. In Ω_d, the porous media flow motion is governed by Darcy's law:

$$\mathbb{K}^{-1} \boldsymbol{u}_d = -\nabla p_d \quad \text{in } \Omega_d, \tag{2.2a}$$

$$\mathrm{div}\, \boldsymbol{u}_d = g \quad \text{in } \Omega_d, \tag{2.2b}$$

$$\boldsymbol{u}_d \cdot \boldsymbol{n}_d = 0 \quad \text{on } \Gamma_d, \tag{2.2c}$$

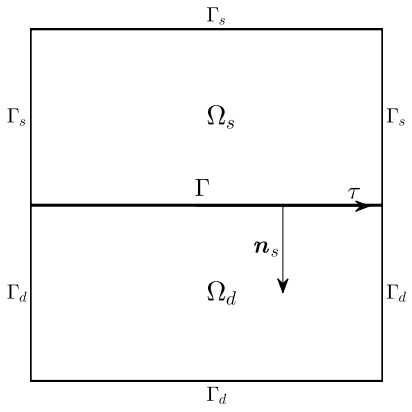

Fig. 1. A sketch of the free fluid domain Ω_s, the porous media domain Ω_d and the interface Γ in two dimensions.

where $\mathbb{K}$ denotes the permeability of the medium, is assumed to be a constant and bounded below. The source term $g \in L^2(\Omega_d)$ is assumed to have zero mean value on Ω_d, so that it is compatible with the boundary condition. The key part of this coupled model is a set of interface conditions that describe how different types of flow interact at the fluid/porous medium interface Γ:

$$\boldsymbol{u}_s \cdot \boldsymbol{n}_s = \boldsymbol{u}_d \cdot \boldsymbol{n}_s, \tag{2.3a}$$

$$-2\nu\epsilon(\boldsymbol{u}_s)\boldsymbol{n}_s \cdot \boldsymbol{n}_s + p_s = p_d, \tag{2.3b}$$

$$-2\nu\epsilon(\boldsymbol{u}_s)\boldsymbol{n}_s \cdot \boldsymbol{\tau}_j = \alpha \boldsymbol{u}_s \cdot \boldsymbol{\tau}_j, \ \ j = 1, \ldots, d-1, \tag{2.3c}$$

where $\boldsymbol{\tau}_j$, $j = 1, \ldots, d-1$, denote the unit tangent vectors on Γ, α is a positive parameter depending on the properties of the porous medium. The conditions (2.3a) and (2.3b) represent the mass conservation and balance of normal stress across the interface, respectively. Eq. (2.3c) is the classical Beavers–Joseph–Saffman (BJS) condition [1,2].

We define two function spaces for the velocity and the pressure as

$$\boldsymbol{V} := \{\boldsymbol{v} \in \boldsymbol{L}^2(\Omega) : \operatorname{div} \boldsymbol{v} \in L^2(\Omega), \boldsymbol{v}|_{\Omega_s} \in \boldsymbol{H}^1(\Omega_s), \boldsymbol{v} = \boldsymbol{0} \text{ on } \Gamma_s, \boldsymbol{v} \cdot \boldsymbol{n}_d = 0 \text{ on } \Gamma_d\},$$

$$Q := L_0^2(\Omega) = \{q \in L^2(\Omega) : \int_\Omega q \, \mathrm{d}\boldsymbol{x} = 0\}.$$

Using integration by parts and the interface conditions (2.3) lead to the weak formulation: Find $\boldsymbol{u} \in \boldsymbol{V}$ and $p \in Q$ such that

$$a(\boldsymbol{u}, \boldsymbol{v}) + b(\boldsymbol{v}, p) = (\boldsymbol{f}, \boldsymbol{v})_{\Omega_s} \quad \forall \mathbf{v} \in \mathbf{V}, \tag{2.4a}$$

$$b(\boldsymbol{u}, q) = -(g, q)_{\Omega_d} \quad \forall q \in Q, \tag{2.4b}$$

where

$$a(\boldsymbol{u}, \boldsymbol{v}) = (2\nu\epsilon(\boldsymbol{u}), \epsilon(\boldsymbol{v}))_{\Omega_s} + (\mathbb{K}^{-1}\boldsymbol{u}, \boldsymbol{v})_{\Omega_d} + \sum_{j=1}^{d-1} \alpha \langle \boldsymbol{u}|_{\Omega_s} \cdot \boldsymbol{\tau}_j, \boldsymbol{v}|_{\Omega_s} \cdot \boldsymbol{\tau}_j \rangle_\Gamma,$$

$$b(\boldsymbol{v}, q) = -(\operatorname{div} \boldsymbol{v}, q),$$

where $\langle \cdot, \cdot \rangle_\Gamma$ denotes $(d-1)-$dimensional inner product on Γ. The well-posedness of problem (2.4) can be found in [14].

3. Weak virtual element space

Let $\mathcal{T}_h$ be a decomposition of Ω into non-overlapping (possibly non-convex) polygons or polyhedra which are aligned with the interface Γ, with characteristic mesh size h, and $\mathcal{F}_h$ be the collection of all the $(d-1)-$dimensional faces. Here we assume that the mesh $\mathcal{T}_h$ is shape regular in the sense that: (1) each element $E \in \mathcal{T}_h$ (and each face

$f \in \mathcal{F}_h$) is star shaped, (2) the diameters of the faces and elements are equivalent $h_f \simeq h_E$. The mesh is also assumed to be quasi-uniform in the sense that the diameters of all the elements are of comparable size. For each element $E \in \mathcal{T}_h$, we define $\boldsymbol{n}_E$ as the unit outward normal vector on ∂E and the subscript will be dropped in a clear case.

Due to the assumption that the elements are not cut by the interface Γ, the partition $\mathcal{T}_h$ can be naturally divided into two sets denoted by $\mathcal{T}_{h,s} = \mathcal{T}_h \cap \overline{\Omega}_s$ and $\mathcal{T}_{h,d} = \mathcal{T}_h \cap \overline{\Omega}_d$. The set of all faces of the decomposition $\mathcal{T}_{h,s}$ is denoted by $\mathcal{F}_{h,s}$. Note that $\mathcal{F}_{h,s}$ includes faces belonging to the interface Γ. We point out that hanging nodes on Γ are allowed in practice, that is to say, the intersection angle between two adjacent faces is allowed to be 180 degree.

As usual, for a positive integer k, P_k denotes the space of polynomials with total degree less than or equal to k, and $\boldsymbol{P}_k$ denotes the corresponding vector polynomial space. For a face f in one dimension with midpoint x_f and length h_f, a basis for $P_k(f)$ is defined as

$$P_k(f) := \left\{1, \frac{x - x_f}{h_f}, \left(\frac{x - x_f}{h_f}\right)^2, \ldots, \left(\frac{x - x_f}{h_f}\right)^k\right\}. \tag{3.1}$$

For a two-dimensional element E with centroid $\boldsymbol{x}_E$ and diameter h_E, a basis for $P_k(E)$ is

$$P_k(E) := \left\{\left(\frac{\boldsymbol{x} - \boldsymbol{x}_E}{h_E}\right)^{\boldsymbol{\alpha}}, |\boldsymbol{\alpha}| \le k\right\}, \tag{3.2}$$

where, for a nonnegative multi-index $\boldsymbol{\alpha} = (\alpha_1, \alpha_2)$, we set $|\boldsymbol{\alpha}| = \alpha_1 + \alpha_2$ and if $\boldsymbol{x} = (x, y)$ then $\boldsymbol{x}^{\boldsymbol{\alpha}} = x^{\alpha_1} y^{\alpha_2}$. Similar notation can be applied in three dimensions.

3.1. $\boldsymbol{H}$(div)-conforming virtual element space

On each element E in $\mathcal{T}_h$, following [46], for every integer $k \ge 1$, a local space is defined as follows, if $d = 2$,

$$\boldsymbol{V}_E := \{\boldsymbol{v} \in \boldsymbol{H}(\mathrm{div}, E) \cap \boldsymbol{H}(\mathrm{rot}, E) : \boldsymbol{v} \cdot \boldsymbol{n} \in P_k(f), \forall f \subset \partial E, \mathrm{div}\, \boldsymbol{v} \in P_{k-1}(E), \mathrm{rot}\, \boldsymbol{v} \in P_{k-1}(E)\},$$

if $d = 3$,

$$\boldsymbol{V}_E := \{\boldsymbol{v} \in \boldsymbol{H}(\mathrm{div}, E) \cap \boldsymbol{H}(\mathbf{curl}, E) : \boldsymbol{v} \cdot \boldsymbol{n} \in P_k(f), \forall f \subset \partial E, \mathrm{div}\, \boldsymbol{v} \in P_{k-1}(E), \mathbf{curl}\, \boldsymbol{v} \in \mathbf{curl}\,(\boldsymbol{P}_k(E))\}.$$

It is easy to check that $\boldsymbol{P}_k(E)$ belongs to $\boldsymbol{V}_E$, which ensures an optimal approximation property of the space. As a completely different approach, compared with the traditional finite element method, there is no explicit expression of a basis function in $\boldsymbol{V}_E$. The degrees of freedom are only used in the assembly process of the matrix, which explains the name virtual element method. By patching $\boldsymbol{V}_E$ over all elements $E \in \mathcal{T}_h$, the following global virtual element space is a conforming discretization to $\boldsymbol{H}(\mathrm{div}, \Omega)$,

$$\boldsymbol{V}_h^{\mathrm{div}} := \{\boldsymbol{v} \in \boldsymbol{H}(\mathrm{div}, \Omega) : \boldsymbol{v} \in \boldsymbol{V}_E, \forall E \in \mathcal{T}_h, \boldsymbol{v} \cdot \boldsymbol{n} = 0 \text{ on } \partial\Omega\},$$

where $\boldsymbol{n}$ denotes the unit outward normal vector on the boundary $\partial\Omega$.

In $\boldsymbol{V}_E$ we define the following degrees of freedom (d.o.f.):

$$\text{Type I} \quad \int_f \boldsymbol{v} \cdot \boldsymbol{n}\, q_k \,\mathrm{d}s \qquad \forall q_k \in P_k(f),\ f \subset \partial E,$$

$$\text{Type II} \quad \int_E \boldsymbol{v} \cdot \boldsymbol{q}_{k-2} \,\mathrm{d}\boldsymbol{x} \quad \forall \boldsymbol{q}_{k-2} \in \nabla P_{k-1}(E),$$

$$\text{Type III} \quad \int_E \boldsymbol{v} \cdot \boldsymbol{q}_k \,\mathrm{d}\boldsymbol{x} \qquad \forall \boldsymbol{q}_k \in (\nabla P_{k+1}(E))^{\perp},$$

where $(\nabla P_{k+1}(E))^{\perp}$ denotes the $\boldsymbol{L}^2$ orthogonal complement of $\nabla P_{k+1}(E)$ in $\boldsymbol{P}_k(E)$. The unisolvence can be found in [46] and thus is skipped here. Fig. 2 shows the d.o.f. of the lowest order element on a polygon in two dimensions. In fact, the three polynomials $\boldsymbol{v} \cdot \boldsymbol{n} \in P_k(f)$, $\mathrm{div}\, \boldsymbol{v} \in P_{k-1}(E)$ and $\mathrm{rot}\, \boldsymbol{v} \in P_{k-1}(E)$ if $d = 2$ (or $\mathbf{curl}\, \boldsymbol{v} \in \mathbf{curl}\,(\boldsymbol{P}_k(E))$ if $d = 3$) are computable using only the degrees of freedom of $\boldsymbol{v}$, see [46] for details.

On each element E, we now define a $\boldsymbol{L}^2$ projection operator $\boldsymbol{\Pi}_E^o$. For each $\boldsymbol{v} \in \boldsymbol{V}_E$, we define $\boldsymbol{\Pi}_E^o \boldsymbol{v} \in \boldsymbol{P}_k(E)$ as

$$\int_E \boldsymbol{\Pi}_E^o \boldsymbol{v} \cdot \boldsymbol{q} \,\mathrm{d}\boldsymbol{x} = \int_E \boldsymbol{v} \cdot \boldsymbol{q} \,\mathrm{d}\boldsymbol{x} \quad \forall \boldsymbol{q} \in \boldsymbol{P}_k(E). \tag{3.3}$$

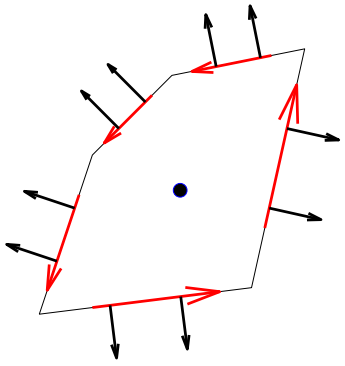

Fig. 2. An illustration of the d.o.f. of the lowest order element ($k = 1$) in two dimensions. The d.o.f. in $\boldsymbol{V}_E$ are colored in black, while the tangential d.o.f. in $\boldsymbol{V}_f$ are colored in red. (For interpretation of the references to color in this figure legend, the reader is referred to the web version of this article.)

For any $\boldsymbol{v} \in \boldsymbol{V}_E$, the $\boldsymbol{L}^2$ projection $\boldsymbol{\Pi}^o_E \boldsymbol{v}$ is actually computable using only its d.o.f. [46]. In consideration of the orthogonal decomposition $\boldsymbol{P}_k(E) = (\nabla P_{k+1}(E))^{\perp} \oplus (\nabla P_{k+1}(E))$ and Type III d.o.f., we need only to determine $\int_E \boldsymbol{v} \cdot \nabla p_{k+1} \, \mathrm{d}\boldsymbol{x}$ which is also computable through integration by parts

$$\int_E \boldsymbol{v} \cdot \nabla p_{k+1} \, \mathrm{d}\boldsymbol{x} = -\int_E \operatorname{div} \boldsymbol{v} \, p_{k+1} \, \mathrm{d}\boldsymbol{x} + \int_{\partial E} \boldsymbol{v} \cdot \boldsymbol{n} \, p_{k+1} \, \mathrm{d}s.$$

As mentioned before, $\boldsymbol{v} \cdot \boldsymbol{n}$ and $\operatorname{div} \boldsymbol{v}$ are known from the d.o.f. of $\boldsymbol{v}$. Therefore, all integral terms on the right-hand side of the above equality are again computable.

3.2. Weak virtual element space

On each $E \in \mathcal{T}_{h,s}$, we use $\mathbf{RM}(E)$ to denote the space of rigid motions,

$$\mathbf{RM}(E) := \{\boldsymbol{c} + R\boldsymbol{x}, \boldsymbol{c} \in \mathbb{R}^d, R \in \mathbb{S}_d\},$$

where $\mathbb{S}_d$ is the space of anti-symmetric $d \times d$ matrices. The trace of the rigid motion on each $f \subset \partial E$ forms a finite dimensional space denoted by

$$\mathbf{RM}(f) := \{\boldsymbol{v} \in \boldsymbol{L}^2(f) : \boldsymbol{v} = \tilde{\boldsymbol{v}}|_f \text{ for some } \tilde{\boldsymbol{v}} \in \mathbf{RM}(E), \, f \subset \partial E\}.$$

We now introduce a space $\boldsymbol{V}_f := \boldsymbol{P}_{k-1}(f) + \mathbf{RM}(f)$ for any $f \in \mathcal{F}_{h,s}$ to involve the tangential part of the velocity. We note that $\boldsymbol{V}_f = \boldsymbol{P}_{k-1}(f)$ for $k > d - 2$. For ease of presentation, we usually express the vector polynomial space $\boldsymbol{V}_f$ in d dimensions, e.g., for all $\boldsymbol{v} \in \boldsymbol{V}_f$, we write it as

$$\boldsymbol{v} = \sum_{j=1,\ldots,d-1} v_j \boldsymbol{\tau}_j, \; v_j \in P_{k-1}(f),$$

where $\boldsymbol{\tau}_j$, $j = 1, \ldots, d-1$, denote orthogonal unit tangential vectors on the face. Then, the element boundary space is defined as

$$\boldsymbol{V}^t_h := \{\boldsymbol{v}^t \in \boldsymbol{L}^2(\mathcal{F}_{h,s}) : \boldsymbol{v}^t|_f \in \boldsymbol{V}_f, \forall f \in \mathcal{F}_{h,s}, \boldsymbol{v}^t = \boldsymbol{0} \text{ on } \Gamma_s\}.$$

Combining the above two kinds of spaces together gives our weak virtual finite element space:

$$\boldsymbol{V}_h := \{\boldsymbol{v}_h = (\boldsymbol{v}^{\mathrm{div}}_h, \boldsymbol{v}^t_h), \boldsymbol{v}^{\mathrm{div}}_h \in \boldsymbol{V}^{\mathrm{div}}_h, \boldsymbol{v}^t_h \in \boldsymbol{V}^t_h\}.$$

We remark that for any $\boldsymbol{v}_h$ in $\boldsymbol{V}_h$, its first part $\boldsymbol{v}^{\mathrm{div}}_h$ is defined in the whole partition $\mathcal{T}_h$, while its second part $\boldsymbol{v}^t_h$ is defined only on $\mathcal{F}_{h,s}$ which is the set of all faces of $\mathcal{T}_{h,s}$, and $\boldsymbol{v}^t_h$ is single valued on each face.

For any $E \in \mathcal{T}_{h,s}$ and its each face f, in order to establish the connection between the $\boldsymbol{H}(\mathrm{div})$-conforming virtual element space $\boldsymbol{V}_E$ and the tangential space $\boldsymbol{V}_f$, we further introduce a projection to the tangential polynomial space

on each element face. On the face $f \subset \partial E$, for each $\boldsymbol{v} \in \boldsymbol{H}^1(E)$, we define $(\boldsymbol{\Pi}^t_{\partial E}\boldsymbol{v})|_f \in \boldsymbol{V}_f$ as

$$\int_f \boldsymbol{\Pi}^t_{\partial E}\boldsymbol{v} \cdot \boldsymbol{q}\,\mathrm{d}s = \int_f \boldsymbol{v}|_E \cdot \boldsymbol{q}\,\mathrm{d}s \quad \forall \boldsymbol{q} \in \boldsymbol{V}_f. \tag{3.4}$$

For the term $\int_f \boldsymbol{v}|_E \cdot \boldsymbol{q}\,\mathrm{d}s$, it is computable if $\boldsymbol{v} \in \boldsymbol{P}_k(E)$; however, it is not computable if $\boldsymbol{v} \in \boldsymbol{V}_E$, since there is no tangential d.o.f. of $\boldsymbol{v}$. In the following definition, the projection $\boldsymbol{\Pi}^t_{\partial E}$ will act on $\boldsymbol{\Pi}^o_E\boldsymbol{v}$ instead of $\boldsymbol{v}$, so that $\int_f \boldsymbol{\Pi}^o_E\boldsymbol{v}|_E \cdot \boldsymbol{q}\,\mathrm{d}s$ is computable.

Let $\boldsymbol{V}_h(E)$ be the restriction of $\boldsymbol{V}_h$ on each element $E \in \mathcal{T}_{h,s}$. Following [44], we now directly give the definition of a weak symmetric gradient for functions in $\boldsymbol{V}_h(E)$. Let $\mathbb{P}^s_{k-1}(E)$ be the space of symmetric matrices, whose components are polynomials of degree at most $k-1$. For any $\boldsymbol{v} = (\boldsymbol{v}^{\mathrm{div}}, \boldsymbol{v}^t) \in \boldsymbol{V}_h(E)$ and any $\mathbb{W} \in \mathbb{P}^s_{k-1}(E)$, we define $\epsilon^w_E(\boldsymbol{v}) \in \mathbb{P}^s_{k-1}(E)$ as

$$(\epsilon^w_E(\boldsymbol{v}), \mathbb{W})_E = (\epsilon(\boldsymbol{\Pi}^o_E\boldsymbol{v}^{\mathrm{div}}), \mathbb{W})_E + \langle \boldsymbol{\Pi}_{\partial E}\mathcal{J}_{\partial E}(\boldsymbol{v}), \mathbb{W}\boldsymbol{n}\rangle_{\partial E}, \tag{3.5}$$

where

$$\begin{aligned}
&\boldsymbol{\Pi}_{\partial E}\boldsymbol{v} := (\boldsymbol{v}\cdot\boldsymbol{n})\boldsymbol{n} + \boldsymbol{\Pi}^t_{\partial E}\boldsymbol{v},\\
&\mathcal{J}_{\partial E}(\boldsymbol{v}) := \mathcal{J}^{\boldsymbol{n}}_{\partial E}(\boldsymbol{v}) + \mathcal{J}^{\boldsymbol{\tau}}_{\partial E}(\boldsymbol{v}) \text{ with } \mathcal{J}^{\boldsymbol{\tau}}_{\partial E}(\boldsymbol{v}) := \sum_{j=1}^{d-1} \mathcal{J}^{\boldsymbol{\tau}_j}_{\partial E}(\boldsymbol{v}),\\
&\mathcal{J}^{\boldsymbol{n}}_{\partial E}(\boldsymbol{v}) := ((\boldsymbol{v}^{\mathrm{div}} - \boldsymbol{\Pi}^o_E\boldsymbol{v}^{\mathrm{div}})\cdot\boldsymbol{n})\boldsymbol{n},\\
&\mathcal{J}^{\boldsymbol{\tau}_j}_{\partial E}(\boldsymbol{v}) := ((\boldsymbol{v}^t - \boldsymbol{\Pi}^o_E\boldsymbol{v}^{\mathrm{div}})\cdot\boldsymbol{\tau}_j)\boldsymbol{\tau}_j \quad j = 1,\ldots,d-1.
\end{aligned}$$

With the help of these notation, we can rewrite $\boldsymbol{\Pi}_{\partial E}\mathcal{J}_{\partial E}(\boldsymbol{v})$ as

$$\boldsymbol{\Pi}_{\partial E}\mathcal{J}_{\partial E}(\boldsymbol{v}) = ((\boldsymbol{v}^{\mathrm{div}} - \boldsymbol{\Pi}^o_E\boldsymbol{v}^{\mathrm{div}})\cdot\boldsymbol{n})\boldsymbol{n} + \sum_{j=1}^{d-1}((\boldsymbol{v}^t - \boldsymbol{\Pi}^t_{\partial E}(\boldsymbol{\Pi}^o_E\boldsymbol{v}^{\mathrm{div}}))\cdot\boldsymbol{\tau}_j)\boldsymbol{\tau}_j.$$

We note that the projection $\boldsymbol{\Pi}^t_{\partial E}$ acts on the polynomial $\boldsymbol{\Pi}^o_E\boldsymbol{v}^{\mathrm{div}}$ but not the virtual function $\boldsymbol{v}^{\mathrm{div}}$ and thus the term $\boldsymbol{\Pi}_{\partial E}\mathcal{J}_{\partial E}(\boldsymbol{v})$ is still computable.

3.3. Interpolation error estimates

On one hand, for every $E \in \mathcal{T}_h$, given any $\boldsymbol{v} \in \boldsymbol{H}^1(E)$, the local interpolation operator $\boldsymbol{I}^{\mathrm{div}}_E : \boldsymbol{H}^1(E) \to \boldsymbol{V}_E$ is defined by the degrees of freedom, i.e.,

$$\int_f \boldsymbol{I}^{\mathrm{div}}_E\boldsymbol{v}\cdot\boldsymbol{n}\,q_k\,\mathrm{d}s = \int_f \boldsymbol{v}\cdot\boldsymbol{n}\,q_k\,\mathrm{d}s \quad \forall q_k \in P_k(f),\ f \subset \partial E, \tag{3.6a}$$

$$\int_E \boldsymbol{I}^{\mathrm{div}}_E\boldsymbol{v}\cdot\boldsymbol{q}_{k-2}\,\mathrm{d}\boldsymbol{x} = \int_E \boldsymbol{v}\cdot\boldsymbol{q}_{k-2}\,\mathrm{d}\boldsymbol{x} \quad \forall \boldsymbol{q}_{k-2} \in \nabla P_{k-1}(E), \tag{3.6b}$$

$$\int_E \boldsymbol{I}^{\mathrm{div}}_E\boldsymbol{v}\cdot\boldsymbol{q}_k\,\mathrm{d}\boldsymbol{x} = \int_E \boldsymbol{v}\cdot\boldsymbol{q}_k\,\mathrm{d}\boldsymbol{x} \quad \forall \boldsymbol{q}_k \in (\nabla P_{k+1}(E))^{\perp}. \tag{3.6c}$$

On the other hand, for any $E \in \mathcal{T}_{h,s}$, the local tangential interpolation operator $\boldsymbol{\Pi}^t_{\partial E}\boldsymbol{v}$ is defined as described in (3.4). Therefore, we can group the above two operators into $\boldsymbol{I}_E\boldsymbol{v} = (\boldsymbol{I}^{\mathrm{div}}_E\boldsymbol{v}, \boldsymbol{\Pi}^t_{\partial E}\boldsymbol{v})$. Note that the second part $\boldsymbol{\Pi}^t_{\partial E}\boldsymbol{v}$ is defined in the free fluid region Ω_s.

Lemma 3.1. *We have for any $\mathbb{W} \in \mathbb{P}^s_{k-1}(E)$ that*

$$(\epsilon(\boldsymbol{v}), \mathbb{W})_E = (\epsilon^w_E(\boldsymbol{I}_E\boldsymbol{v}), \mathbb{W})_E, \tag{3.7}$$

where $\boldsymbol{I}_E\boldsymbol{v} = (\boldsymbol{I}^{div}_E\boldsymbol{v}, \boldsymbol{\Pi}^t_{\partial E}\boldsymbol{v})$.

Proof. The proof follows directly from the definitions of the weak symmetric gradient and the interpolation, i.e., (3.5) and (3.6). □

Throughout the paper, we employ the expression $a \lesssim b$ to denote that there exists a positive constant C independent of the mesh size h such that $a \leq Cb$. But C may depend on ν, $\mathbb{K}$ or α. We also use $a \simeq b$ to denote that a and b are equivalent. Under the mesh assumptions, some standard techniques still hold [47,48], e.g., the inverse inequality, the trace theorem, the Bramble–Hilbert lemma. The stability of the interpolating operator can be found in [49]. Here we summarize the following error estimates contained in [44].

Lemma 3.2. *Suppose that the element E is shape regular. Then, for all $\boldsymbol{v} \in \boldsymbol{H}^{k+1}(E)$, the following estimates hold true for the operators $\boldsymbol{I}_E = (\boldsymbol{I}_E^{div}, \boldsymbol{\Pi}_{\partial E}^t)$ and $\boldsymbol{\Pi}_E^o$*

$$\|\boldsymbol{v} - \boldsymbol{\Pi}_E^o \boldsymbol{v}\|_E + h\|\nabla(\boldsymbol{v} - \boldsymbol{\Pi}_E^o \boldsymbol{v})\|_E + h^{\frac{1}{2}}\|\boldsymbol{v} - \boldsymbol{\Pi}_E^o \boldsymbol{v}\|_{\partial E} \lesssim h^{k+1}\|\boldsymbol{v}\|_{k+1,E}, \tag{3.8a}$$

$$\|\boldsymbol{v} - \boldsymbol{I}_E^{div} \boldsymbol{v}\|_E + \|\boldsymbol{v} - \boldsymbol{\Pi}_E^o \boldsymbol{I}_E^{div} \boldsymbol{v}\|_E + h\|\nabla(\boldsymbol{v} - \boldsymbol{\Pi}_E^o \boldsymbol{I}_E^{div} \boldsymbol{v})\|_E \lesssim h^{k+1}\|\boldsymbol{v}\|_{k+1,E}, \tag{3.8b}$$

$$\|\boldsymbol{\Pi}_{\partial E} \mathcal{J}_{\partial E}(\boldsymbol{I}_E \boldsymbol{v})\|_{\partial E} \lesssim h^{k+\frac{1}{2}}\|\boldsymbol{v}\|_{k+1,E}, \tag{3.8c}$$

$$\|\epsilon(\boldsymbol{v}) - \epsilon_E^w(\boldsymbol{I}_E \boldsymbol{v})\|_E + h\|\epsilon(\boldsymbol{v}) - \epsilon_E^w(\boldsymbol{I}_E \boldsymbol{v})\|_{1,E} \lesssim h^k\|\boldsymbol{v}\|_{k+1,E}. \tag{3.8d}$$

When the subscript E is replaced by the mesh size h, the operators introduced above are element-wise defined on corresponding domain, i.e., $(\epsilon_h^w(\cdot))|_E = \epsilon_E^w(\cdot)$, $\boldsymbol{\Pi}_h^o|_E = \boldsymbol{\Pi}_E^o$, $\boldsymbol{I}_h^{\text{div}}|_E = \boldsymbol{I}_E^{\text{div}}$, $\boldsymbol{\Pi}_h^t|_E = \boldsymbol{\Pi}_{\partial E}^t$, $\boldsymbol{I}_h|_E = \boldsymbol{I}_E$. The interpolation to $\boldsymbol{V}_h$ is defined as $\boldsymbol{I}_h = (\boldsymbol{I}_h^{\text{div}}, \boldsymbol{\Pi}_h^t)$.

4. The discrete problem and its well-posedness

4.1. Discretization

Let $Q_h \subset L_0^2(\Omega)$ be a discontinuous piecewise P_{k-1} element space. Then, the corresponding discrete variational formulation reads as follows: Find $\boldsymbol{u}_h = (\boldsymbol{u}_h^{\text{div}}, \boldsymbol{u}_h^t) \in \boldsymbol{V}_h$ and $p_h \in Q_h$ such that

$$a_h(\boldsymbol{u}_h, \boldsymbol{v}_h) + b(\boldsymbol{v}_h, p_h) = (\boldsymbol{f}, \boldsymbol{\Pi}_h^o \boldsymbol{v}_h^{\text{div}})_{\Omega_s} \quad \forall \boldsymbol{v}_h \in \boldsymbol{V}_h, \tag{4.1a}$$

$$b(\boldsymbol{u}_h, q_h) = -(g, q_h)_{\Omega_d} \quad \forall q_h \in Q_h, \tag{4.1b}$$

where

$$\begin{aligned} a_h(\boldsymbol{u}_h, \boldsymbol{v}_h) :&= (2\nu\epsilon_h^w(\boldsymbol{u}_h), \epsilon_h^w(\boldsymbol{v}_h))_{\Omega_s} + 2\nu s_1(\boldsymbol{u}_h, \boldsymbol{v}_h) + \sum_{j=1}^{d-1} \alpha \langle \boldsymbol{u}_h^t \cdot \boldsymbol{\tau}_j, \boldsymbol{v}_h^t \cdot \boldsymbol{\tau}_j \rangle_\Gamma \\ &+ (\mathbb{K}^{-1}\boldsymbol{\Pi}_h^o \boldsymbol{u}_h^{\text{div}}, \boldsymbol{\Pi}_h^o \boldsymbol{v}_h^{\text{div}})_{\Omega_d} + \mathbb{K}^{-1} s_2(\boldsymbol{u}_h^{\text{div}}, \boldsymbol{v}_h^{\text{div}}), \\ b(\boldsymbol{v}_h, q_h) :&= -(\text{div}\, \boldsymbol{v}_h^{\text{div}}, q_h), \end{aligned}$$

and $s_1(\cdot,\cdot)$ and $s_2(\cdot,\cdot)$ are stabilization terms defined as

$$s_1(\boldsymbol{u}_h, \boldsymbol{v}_h) = \sum_{E \in \mathcal{T}_{h,s}} \left\langle h^{-1} \boldsymbol{\Pi}_{\partial E} \mathcal{J}_{\partial E}(\boldsymbol{u}_h), \boldsymbol{\Pi}_{\partial E} \mathcal{J}_{\partial E}(\boldsymbol{v}_h) \right\rangle_{\partial E},$$

$$s_2(\boldsymbol{u}_h^{\text{div}}, \boldsymbol{v}_h^{\text{div}}) = \sum_{E \in \mathcal{T}_{h,d}} \mathcal{D}^E((I - \boldsymbol{\Pi}_h^o)\boldsymbol{u}_h^{\text{div}}, (I - \boldsymbol{\Pi}_h^o)\boldsymbol{v}_h^{\text{div}}),$$

where $\mathcal{D}^E$ is the identity matrix with respect to the local basis determined by the d.o.f. (see [45]).

For any $\boldsymbol{v}_h = (\boldsymbol{v}_h^{\text{div}}, \boldsymbol{v}_h^t) \in \boldsymbol{V}_h$, we define a mesh dependent $\boldsymbol{H}^1$ seminorm as follows

$$|||\boldsymbol{v}_h|||^2 := |||\boldsymbol{v}_h|||_{\Omega_s}^2 + |||\boldsymbol{v}_h|||_{\Omega_d}^2, \tag{4.2}$$

with

$$|||\boldsymbol{v}_h|||_{\Omega_s}^2 = \sum_{E \in \mathcal{T}_{h,s}} \left(2\nu\|\epsilon_h^w(\boldsymbol{v}_h)\|_E^2 + 2\nu h^{-1}\|\boldsymbol{\Pi}_{\partial E} \mathcal{J}_{\partial E}(\boldsymbol{v}_h)\|_{\partial E}^2 + \sum_{j=1}^{d-1} \alpha \|\boldsymbol{v}_h^t \cdot \boldsymbol{\tau}_j\|_{\partial E \cap \Gamma}^2 \right),$$

$$|||\boldsymbol{v}_h|||_{\Omega_d}^2 = \mathbb{K}^{-1}\|\boldsymbol{\Pi}_h^o \boldsymbol{v}_h^{\text{div}}\|_{\Omega_d}^2 + \mathbb{K}^{-1} s_2(\boldsymbol{v}_h^{\text{div}}, \boldsymbol{v}_h^{\text{div}}) + \|\text{div}\, \boldsymbol{v}_h^{\text{div}}\|_{\Omega_d}^2.$$

In the following, we first present a technical lemma, and then give the Poincaré and the Korn inequalities, respectively. Proofs of the following three lemmas have been reported in [44].

Lemma 4.1. *On each element $E \in \mathcal{T}_{h,s}$, we have for any $\boldsymbol{v}_h = (\boldsymbol{v}_h^{div}, \boldsymbol{v}_h^t) \in \boldsymbol{V}_h$ that*

$$\|\boldsymbol{v}_h^{\mathrm{div}} - \boldsymbol{\Pi}_E^o \boldsymbol{v}_h^{\mathrm{div}}\|_E^2 \lesssim h \|\mathcal{J}_{\partial E}^{\boldsymbol{n}}(\boldsymbol{v}_h^{\mathrm{div}})\|_{\partial E}^2, \tag{4.3a}$$

$$\|\mathcal{J}_{\partial E}(\boldsymbol{v}_h)\|_{\partial E}^2 \lesssim \|\boldsymbol{\Pi}_{\partial E}\mathcal{J}_{\partial E}(\boldsymbol{v}_h)\|_{\partial E}^2 + h\|\epsilon(\boldsymbol{\Pi}_E^o \boldsymbol{v}_h^{\mathrm{div}})\|_E^2. \tag{4.3b}$$

Lemma 4.2. *For any $\boldsymbol{v}_h \in \boldsymbol{V}_h$, we have the Poincaré inequality:*

$$\|\boldsymbol{v}_h^{\mathrm{div}}\|_{\Omega_s}^2 \lesssim \sum_{E\in\mathcal{T}_{h,s}} \left(\|\nabla \boldsymbol{\Pi}_E^o \boldsymbol{v}_h^{\mathrm{div}}\|_E^2 + h^{-1}\|\boldsymbol{\Pi}_{\partial E}\mathcal{J}_{\partial E}(\boldsymbol{v}_h)\|_{\partial E}^2 \right). \tag{4.4}$$

Lemma 4.3. *The Korn inequality holds for any $\boldsymbol{v}_h \in \boldsymbol{V}_h$ that*

$$\sum_{E\in\mathcal{T}_{h,s}} \|\nabla \boldsymbol{\Pi}_E^o \boldsymbol{v}_h^{\mathrm{div}}\|_E^2 \lesssim \|\epsilon_h^w(\boldsymbol{v}_h)\|^2 + \sum_{E\in\mathcal{T}_{h,s}} h^{-1}\|\boldsymbol{\Pi}_{\partial E}\mathcal{J}_{\partial E}(\boldsymbol{v}_h)\|_{\partial E}^2. \tag{4.5}$$

We then give a norm equivalence result below.

Lemma 4.4. *For any $\boldsymbol{v}_h = (\boldsymbol{v}_h^{\mathrm{div}}, \boldsymbol{v}_h^t) \in \boldsymbol{V}_h$, it holds that*

$$\mathbb{K}^{-1}\|\boldsymbol{v}_h^{\mathrm{div}}\|_{\Omega_d}^2 \lesssim (\mathbb{K}^{-1}\boldsymbol{\Pi}_h^o \boldsymbol{v}_h^{\mathrm{div}}, \boldsymbol{\Pi}_h^o \boldsymbol{v}_h^{\mathrm{div}})_{\Omega_d} + \mathbb{K}^{-1} s_2(\boldsymbol{v}_h^{\mathrm{div}}, \boldsymbol{v}_h^{\mathrm{div}}) \lesssim \mathbb{K}^{-1}\|\boldsymbol{v}_h^{\mathrm{div}}\|_{\Omega_d}^2. \tag{4.6}$$

Proof. As discussed in [45], the bases (3.1) and (3.2) were chosen such that each of the degrees of freedom in Type I, II and III scales like $\boldsymbol{v}_h^{\mathrm{div}}$ times h_E. So that, the sum of their squares will scale like $\|\boldsymbol{v}_h^{\mathrm{div}}\|_{0,E}^2$. As a consequence, the bilinear form $s_2(\boldsymbol{v}_h^{\mathrm{div}}, \boldsymbol{v}_h^{\mathrm{div}})$ will scale as $\|(I - \boldsymbol{\Pi}_h^o)\boldsymbol{v}_h^{\mathrm{div}}\|_{\Omega_d}^2$. We then have from the definition (3.3) that

$$\begin{aligned}
\mathbb{K}^{-1}\|\boldsymbol{v}_h^{\mathrm{div}}\|_{\Omega_d}^2 &= \mathbb{K}^{-1}\|\boldsymbol{v}_h^{\mathrm{div}} - \boldsymbol{\Pi}_h^o \boldsymbol{v}_h^{\mathrm{div}} + \boldsymbol{\Pi}_h^o \boldsymbol{v}_h^{\mathrm{div}}\|_{\Omega_d}^2 \\
&= \mathbb{K}^{-1}\|\boldsymbol{\Pi}_h^o \boldsymbol{v}_h^{\mathrm{div}}\|_{\Omega_d}^2 + \mathbb{K}^{-1}\|\boldsymbol{v}_h^{\mathrm{div}} - \boldsymbol{\Pi}_h^o \boldsymbol{v}_h^{\mathrm{div}}\|_{\Omega_d}^2 \\
&\simeq \mathbb{K}^{-1}\|\boldsymbol{\Pi}_h^o \boldsymbol{v}_h^{\mathrm{div}}\|_{\Omega_d}^2 + \mathbb{K}^{-1} s_2(\boldsymbol{v}_h^{\mathrm{div}}, \boldsymbol{v}_h^{\mathrm{div}}).
\end{aligned}$$

The proof is completed. □

Lemma 4.5. *The seminorm $|||\cdot|||$, as defined in (4.2), is a norm in the finite dimensional space $\boldsymbol{V}_h$.*

Proof. We only need to check the positivity property of the seminorm $|||\cdot|||$. To this end, suppose that $|||\boldsymbol{v}_h||| = 0$ for some $\boldsymbol{v}_h = (\boldsymbol{v}_h^{\mathrm{div}}, \boldsymbol{v}_h^t) \in \boldsymbol{V}_h$. We first obtain $\boldsymbol{v}_h^{\mathrm{div}}|_{\Omega_d} = \boldsymbol{0}$ from $|||\boldsymbol{v}_h|||_{\Omega_d} = 0$ and Lemma 4.4. Then, we have that $\boldsymbol{v}_h^{\mathrm{div}}|_{\Omega_s} = \boldsymbol{0}$ from the Korn inequality (4.5), the Poincaré inequality (4.4) and the facts $\epsilon_E^w(\boldsymbol{v}_h) = 0$, $\boldsymbol{\Pi}_{\partial E}\mathcal{J}_{\partial E}(\boldsymbol{v}_h) = 0$ for any $E \in \mathcal{T}_{h,s}$. In addition, on the boundary ∂E, it holds that $(\boldsymbol{v}_h^t - \boldsymbol{\Pi}_{\partial E}^t(\boldsymbol{\Pi}_E^o \boldsymbol{v}_h^{\mathrm{div}})) \cdot \boldsymbol{\tau}_j = 0$, which implies that $\boldsymbol{v}_h^t$ equals zero on $\mathcal{F}_{h,s}$. Finally, we achieve the desired result $\boldsymbol{v}_h = \boldsymbol{0}$. □

4.2. The well-posedness of the discrete problem

In this subsection, we shall prove that both $a_h(\cdot,\cdot)$ and $b(\cdot,\cdot)$ are continuous, $a_h(\cdot,\cdot)$ is coercive in the discrete kernel of $\boldsymbol{V}_h$ and $b(\cdot,\cdot)$ satisfies the discrete inf–sup condition. Therefore, the discrete problem (4.1) has a unique solution.

Lemma 4.6. *For any $\boldsymbol{u}_h, \boldsymbol{v}_h \in \boldsymbol{V}_h$ and $q_h \in Q_h$, the two bilinear forms $a_h(\cdot,\cdot)$ and $b(\cdot,\cdot)$ have following upper bounds, i.e.,*

$$a_h(\boldsymbol{u}_h, \boldsymbol{v}_h) \lesssim |||\boldsymbol{u}_h||| \cdot |||\boldsymbol{v}_h|||, \tag{4.7a}$$

$$b(\boldsymbol{v}_h, q_h) \lesssim b^* |||\boldsymbol{v}_h||| \cdot \|q_h\|, \tag{4.7b}$$

where $b^* = \max\left\{\frac{1}{\sqrt{\nu}}, 1\right\}$ is a positive constant.

Proof. The Cauchy–Schwarz inequality and the definition (4.2) of the norm yield the first inequality (4.7a). On one hand, for any $E \in \mathcal{T}_{h,s}$, by integration by parts and the property of $\boldsymbol{L}^2$ projection, we have

$$\begin{aligned}\|\operatorname{div} \boldsymbol{v}_h^{\mathrm{div}} - \operatorname{div} \boldsymbol{\Pi}_h^o \boldsymbol{v}_h^{\mathrm{div}}\|_E^2 &= \int_{\partial E} \operatorname{div}(\boldsymbol{v}_h^{\mathrm{div}} - \boldsymbol{\Pi}_h^o \boldsymbol{v}_h^{\mathrm{div}})(\boldsymbol{v}_h^{\mathrm{div}} - \boldsymbol{\Pi}_h^o \boldsymbol{v}_h^{\mathrm{div}}) \cdot \boldsymbol{n} \mathrm{d}s \\ &\leq \|\mathcal{J}_{\partial E}^{\boldsymbol{n}}(\boldsymbol{v}_h^{\mathrm{div}})\|_{\partial E} \|\operatorname{div}(\boldsymbol{v}_h^{\mathrm{div}} - \boldsymbol{\Pi}_h^o \boldsymbol{v}_h^{\mathrm{div}})\|_{\partial E}.\end{aligned}$$

The trace inequality and the fact $\operatorname{div}(\boldsymbol{v}_h^{\mathrm{div}} - \boldsymbol{\Pi}_h^o \boldsymbol{v}_h^{\mathrm{div}}) \in P_{k-1}(E)$ give that

$$\begin{aligned}\|\operatorname{div}(\boldsymbol{v}_h^{\mathrm{div}} - \boldsymbol{\Pi}_h^o \boldsymbol{v}_h^{\mathrm{div}})\|_{\partial E}^2 &\lesssim h^{-1} \|\operatorname{div}(\boldsymbol{v}_h^{\mathrm{div}} - \boldsymbol{\Pi}_h^o \boldsymbol{v}_h^{\mathrm{div}})\|_E^2 + h \|\nabla \operatorname{div}(\boldsymbol{v}_h^{\mathrm{div}} - \boldsymbol{\Pi}_h^o \boldsymbol{v}_h^{\mathrm{div}})\|_E^2 \\ &\lesssim h^{-1} \|\operatorname{div}(\boldsymbol{v}_h^{\mathrm{div}} - \boldsymbol{\Pi}_h^o \boldsymbol{v}_h^{\mathrm{div}})\|_E^2.\end{aligned}$$

Then, it follows that

$$\|\operatorname{div} \boldsymbol{v}_h^{\mathrm{div}} - \operatorname{div} \boldsymbol{\Pi}_h^o \boldsymbol{v}_h^{\mathrm{div}}\|_E \lesssim h^{-\frac{1}{2}} \|\mathcal{J}_{\partial E}^{\boldsymbol{n}}(\boldsymbol{v}_h^{\mathrm{div}})\|_{\partial E}.$$

By summing over E in $\mathcal{T}_{h,s}$, and using the triangle inequality and the Korn inequality (4.5), we obtain

$$\begin{aligned}b(\boldsymbol{v}_h, q_h) &\leq (\|\operatorname{div}(\boldsymbol{v}_h^{\mathrm{div}} - \boldsymbol{\Pi}_h^o \boldsymbol{v}_h^{\mathrm{div}})\|_{\Omega_s} + \|\operatorname{div} \boldsymbol{\Pi}_h^o \boldsymbol{v}_h^{\mathrm{div}}\|_{\Omega_s}) \|q_h\|_{\Omega_s} \\ &\lesssim \frac{1}{\sqrt{\nu}} |||\boldsymbol{v}_h|||_{\Omega_s} \|q_h\|_{\Omega_s}.\end{aligned}$$

On the other hand, for any $E \in \mathcal{T}_{h,d}$, the inequality (4.7b) follows directly from the Cauchy–Schwarz inequality. Finally, we complete the proof by collecting these two cases. □

Define the discrete kernels of the space $\boldsymbol{V}_h$ as

$$\begin{aligned}\boldsymbol{Z}_h(g) &:= \{\boldsymbol{v}_h \in \boldsymbol{V}_h : b(\boldsymbol{v}_h, q_h) = -(g, q_h)_{\Omega_d}, \forall q_h \in Q_h\}, \\ \boldsymbol{Z}_h &:= \boldsymbol{Z}_h(0) = \{\boldsymbol{v}_h \in \boldsymbol{V}_h : b(\boldsymbol{v}_h, q_h) = 0, \forall q_h \in Q_h\}.\end{aligned}$$

Hence, for any $\boldsymbol{v}_h \in \boldsymbol{Z}_h$ we easily see that $\operatorname{div} \boldsymbol{v}_h^{\mathrm{div}} = 0$.

Lemma 4.7. *The bilinear form $a_h(\cdot, \cdot)$ is $\boldsymbol{Z}_h$-elliptic, i.e.,*

$$a_h(\boldsymbol{v}_h, \boldsymbol{v}_h) = |||\boldsymbol{v}_h|||^2 \quad \forall \boldsymbol{v}_h \in \boldsymbol{Z}_h. \tag{4.8}$$

Proof. Using the fact $\operatorname{div} \boldsymbol{v}_h^{\mathrm{div}} = 0$ in $\boldsymbol{Z}_h$ directly gives the desired result. □

Lemma 4.8. *The bilinear form $b(\cdot, \cdot)$ satisfies the discrete inf–sup condition, i.e.,*

$$\sup_{\boldsymbol{v}_h \in \boldsymbol{V}_h} \frac{b(\boldsymbol{v}_h, q_h)}{|||\boldsymbol{v}_h|||} \gtrsim b_* \|q_h\| \quad \forall q_h \in Q_h, \tag{4.9}$$

where $b_* = \sqrt{\min\left\{\mathbb{K}, \frac{1}{\nu}, \frac{1}{\alpha}\right\}}$ is a positive constant.

Proof. It is well known that for any $q_h \in Q_h$, there exists a function $\boldsymbol{v} \in \boldsymbol{H}_0^1(\Omega)$ satisfying

$$\operatorname{div} \boldsymbol{v} = q_h \text{ and } \|\boldsymbol{v}\|_{1,\Omega} \lesssim \|q_h\|.$$

We define $\boldsymbol{v}_h = (\boldsymbol{v}_h^{\mathrm{div}}, \boldsymbol{v}_h^t)$ as $\boldsymbol{v}_h^{\mathrm{div}}|_E = \boldsymbol{I}_E^{\mathrm{div}} \boldsymbol{v}$ on $E \in \mathcal{T}_h$ and $\boldsymbol{v}_h^t|_{\partial E} = \boldsymbol{\Pi}_{\partial E}^t \boldsymbol{v}$ on $E \in \mathcal{T}_{h,s}$. Then, for any $q \in P_{k-1}$ on $E \in \mathcal{T}_h$, we have

$$\int_E \operatorname{div} \boldsymbol{v}_h^{\mathrm{div}}\, q \,\mathrm{d}\boldsymbol{x} = -\int_E \boldsymbol{v}_h^{\mathrm{div}} \nabla q \,\mathrm{d}\boldsymbol{x} + \int_{\partial E} \boldsymbol{v}_h^{\mathrm{div}} \cdot \boldsymbol{n}\, q \,\mathrm{d}s = -\int_E \boldsymbol{v} \nabla q \,\mathrm{d}\boldsymbol{x} + \int_{\partial E} \boldsymbol{v} \cdot \boldsymbol{n}\, q \,\mathrm{d}s = \int_E \operatorname{div} \boldsymbol{v}\, q \,\mathrm{d}\boldsymbol{x}.$$

By noting that $\operatorname{div} \boldsymbol{v} = q_h \in P_{k-1}(E)$, we obtain the equality

$$\operatorname{div} \boldsymbol{v}_h^{\mathrm{div}} = q_h.$$

With $\boldsymbol{v}_h$ restricted to Ω_d, according to the inequality (3.8b), we deduce

$$\|\boldsymbol{v}_h^{\mathrm{div}}\|_{\Omega_d} \leq \|\boldsymbol{v}\|_{\Omega_d} + \|\boldsymbol{v} - \boldsymbol{v}_h^{\mathrm{div}}\|_{\Omega_d} \lesssim \|\boldsymbol{v}\|_{1,\Omega_d}.$$

Then, when $\boldsymbol{v}_h$ restricted to Ω_s, it follows from the triangle inequality and (3.8d) that

$$\|\epsilon_h^w(\boldsymbol{v}_h)\|_{\Omega_s} \leq \|\epsilon_h^w(\boldsymbol{v}_h) - \epsilon(\boldsymbol{v})\|_{\Omega_s} + \|\epsilon(\boldsymbol{v})\|_{\Omega_s} \lesssim \|\boldsymbol{v}\|_{1,\Omega_s}.$$

By using the inequality (3.8c), it holds that

$$\sum_{E\in\mathcal{T}_{h,s}} h^{-1}\|\boldsymbol{\Pi}_{\partial E}\mathcal{J}_{\partial E}(\boldsymbol{v}_h)\|_{\partial E}^2 \lesssim \sum_{E\in\mathcal{T}_{h,s}} \|\boldsymbol{v}\|_{1,E}^2 = \|\boldsymbol{v}\|_{1,\Omega_s}^2.$$

For the tangential part in the definition of the norm, we apply the trace theorem to arrive

$$\sum_{E\in\mathcal{T}_{h,s}}\sum_{j=1}^{d-1} \|\boldsymbol{v}_h^t\cdot\boldsymbol{\tau}_j\|_{\partial E\cap\Gamma}^2 \lesssim \sum_{E\in\mathcal{T}_{h,s}} \|\boldsymbol{v}\|_{\partial E\cap\Gamma}^2 \lesssim \|\boldsymbol{v}\|_{\Gamma}^2 \lesssim \|\boldsymbol{v}\|_{1,\Omega_s}^2.$$

Summing over the above inequalities and applying the equality $\operatorname{div}\boldsymbol{v}_h^{\mathrm{div}} = q_h$, we obtain

$$\sqrt{\min\left\{\mathbb{K}, \frac{1}{\nu}, \frac{1}{\alpha}\right\}}|||\boldsymbol{v}_h||| \lesssim \|q_h\|,$$

and therefore, we derive that

$$\sup_{\boldsymbol{v}_h\in\boldsymbol{V}_h} \frac{|b(\boldsymbol{v}_h, q_h)|}{|||\boldsymbol{v}_h|||} = \sup_{\boldsymbol{v}_h\in\boldsymbol{V}_h} \frac{|(\operatorname{div}\boldsymbol{v}_h^{\mathrm{div}}, q_h)|}{|||\boldsymbol{v}_h|||} = \sup_{\boldsymbol{v}_h\in\boldsymbol{V}_h} \frac{\|q_h\|^2}{|||\boldsymbol{v}_h|||} \gtrsim b_*\|q_h\|,$$

where $b_* = \sqrt{\min\left\{\mathbb{K}, \frac{1}{\nu}, \frac{1}{\alpha}\right\}}$. This concludes the proof. □

From Lemmas 4.6–4.8, and the standard framework for saddle point problem [13], we conclude the well-posedness of the discrete problem.

Theorem 4.9. *There exists a unique solution* $(\boldsymbol{u}_h, p_h) \in \boldsymbol{V}_h \times Q_h$ *to problem* (4.1) *such that*

$$|||\boldsymbol{u}_h||| + \|p_h\| \lesssim \|\boldsymbol{\Pi}_h^o\boldsymbol{f}\|_{\Omega_s} + \|g\|_{\Omega_d}. \tag{4.10}$$

5. Error analysis

The purpose of this section is to derive error estimates of $\boldsymbol{u}_h$ in the $|||\cdot|||$-norm and p_h in the standard L^2 norm. To this end, let $(\boldsymbol{u}, p)$ be the solution to (2.1)–(2.3). Then, we define the interpolation $\boldsymbol{u}_I = (\boldsymbol{u}_I^{\mathrm{div}}, \boldsymbol{u}_I^t)$ as $\boldsymbol{u}_I^{\mathrm{div}}|_E = \boldsymbol{I}_E^{\mathrm{div}}\boldsymbol{u}$, $\boldsymbol{u}_I^t|_{\partial E} = \boldsymbol{\Pi}_{\partial E}^t\boldsymbol{u}$, $p_I = P_h p$, where P_h denotes the L^2 projection to the space Q_h. We will derive the upper bounds of $\boldsymbol{u}_h - \boldsymbol{u}_I$ and $p_h - p_I$.

To derive the error equation (5.5), only minimum regularity for the solution is used. To get the optimal error estimates, however, we need more regularity, i.e., $\boldsymbol{u}_s \in \boldsymbol{H}^{k+1}(\Omega_s)$, $\boldsymbol{u}_d \in \boldsymbol{H}^k(\Omega_d)$ and $p \in H^k(\Omega)$, which in turn requires the interface Γ is smooth enough.

5.1. Error equation

Let $\boldsymbol{v}_h = (\boldsymbol{v}_h^{\mathrm{div}}, \boldsymbol{v}_h^t) \in \boldsymbol{Z}_h$, then we have $\operatorname{div}\boldsymbol{v}_h^{\mathrm{div}} = 0$. We compute $a_h(\boldsymbol{u}_h, \boldsymbol{v}_h)$ by using the integration by parts and Eqs. (2.1a), (2.2a), (4.1a),

$$\begin{aligned}
a_h(\boldsymbol{u}_h, \boldsymbol{v}_h) &= (\boldsymbol{f}, \boldsymbol{\Pi}_h^o\boldsymbol{v}_h^{\mathrm{div}})_{\Omega_s} + (\operatorname{div}\boldsymbol{v}_h^{\mathrm{div}}, p_h)\\
&= (\boldsymbol{f}, \boldsymbol{\Pi}_h^o\boldsymbol{v}_h^{\mathrm{div}})_{\Omega_s} + (\operatorname{div}\boldsymbol{v}_h^{\mathrm{div}}, p)\\
&= (\boldsymbol{f}, \boldsymbol{\Pi}_h^o\boldsymbol{v}_h^{\mathrm{div}})_{\Omega_s} - (\boldsymbol{v}_h^{\mathrm{div}}, \nabla p)_{\Omega_s} - (\boldsymbol{v}_h^{\mathrm{div}}, \nabla p)_{\Omega_d} + \langle p_s - p_d, \boldsymbol{v}_h^{\mathrm{div}}\cdot\boldsymbol{n}_s\rangle_{\Gamma}\\
&= (\boldsymbol{f} + 2\nu\operatorname{div}\epsilon(\boldsymbol{u}), \boldsymbol{\Pi}_h^o\boldsymbol{v}_h^{\mathrm{div}} - \boldsymbol{v}_h^{\mathrm{div}})_{\Omega_s} + (\mathbb{K}^{-1}\boldsymbol{u}, \boldsymbol{v}_h^{\mathrm{div}})_{\Omega_d} - (2\nu\operatorname{div}\epsilon(\boldsymbol{u}), \boldsymbol{\Pi}_h^o\boldsymbol{v}_h^{\mathrm{div}})_{\Omega_s}\\
&\quad + \langle p_s - p_d, \boldsymbol{v}_h^{\mathrm{div}}\cdot\boldsymbol{n}_s\rangle_{\Gamma}.
\end{aligned} \tag{5.1}$$

We further simplify the third term on the right-hand side of (5.1). It follows from integration by parts that

$$\begin{aligned}(-2\nu\mathrm{div}\,\epsilon(\boldsymbol{u}),\boldsymbol{\Pi}_h^o\boldsymbol{v}_h^{\mathrm{div}})_{\Omega_s} &= (2\nu\epsilon(\boldsymbol{u}),\epsilon(\boldsymbol{\Pi}_h^o\boldsymbol{v}_h^{\mathrm{div}}))_{\Omega_s} - \sum_{E\in\mathcal{T}_{h,s}}\left\langle 2\nu\epsilon(\boldsymbol{u})\boldsymbol{n},\boldsymbol{\Pi}_h^o\boldsymbol{v}_h^{\mathrm{div}}\right\rangle_{\partial E}\\ &= (2\nu\epsilon(\boldsymbol{u}),\epsilon(\boldsymbol{\Pi}_h^o\boldsymbol{v}_h^{\mathrm{div}}))_{\Omega_s} + \sum_{E\in\mathcal{T}_{h,s}}\left\langle 2\nu\epsilon(\boldsymbol{u})\boldsymbol{n},\mathcal{J}_{\partial E}(\boldsymbol{v}_h)\right\rangle_{\partial E}\\ &\quad - \sum_{E\in\mathcal{T}_{h,s}}\left\langle 2\nu\epsilon(\boldsymbol{u})\boldsymbol{n},(\boldsymbol{v}_h^{\mathrm{div}}\cdot\boldsymbol{n})\boldsymbol{n}+\sum_{j=1}^{d-1}(\boldsymbol{v}_h^t\cdot\boldsymbol{\tau}_j)\boldsymbol{\tau}_j\right\rangle_{\partial E\cap\Gamma},\end{aligned}\tag{5.2}$$

where we have used the properties that both $\boldsymbol{v}_h^{\mathrm{div}}\cdot\boldsymbol{n}$ and $\boldsymbol{v}_h^t$ are single valued on the faces in Ω_s and vanish on the outer boundary Γ_s. Now we compute $a_h(\boldsymbol{u}_I,\boldsymbol{v}_h)$. By using another version of weak symmetric gradient ϵ_h^w (see [44]), we have

$$\begin{aligned}(-2\nu\epsilon_h^w(\boldsymbol{u}_I),\epsilon_h^w(\boldsymbol{v}_h))_{\Omega_s} &= (-2\nu\epsilon_h^w(\boldsymbol{u}_I),\epsilon(\boldsymbol{\Pi}_h^o\boldsymbol{v}_h^{\mathrm{div}}))_{\Omega_s} + (-2\nu\epsilon_h^w(\boldsymbol{u}_I),\epsilon_h^w(\boldsymbol{v}_h)-\epsilon(\boldsymbol{\Pi}_h^o\boldsymbol{v}_h^{\mathrm{div}}))_{\Omega_s}\\ &= (-2\nu\epsilon_h^w(\boldsymbol{u}_I),\epsilon(\boldsymbol{\Pi}_h^o\boldsymbol{v}_h^{\mathrm{div}}))_{\Omega_s} + \sum_{E\in\mathcal{T}_{h,s}}\left\langle -2\nu\epsilon_h^w(\boldsymbol{u}_I)\boldsymbol{n},\mathcal{J}_{\partial E}(\boldsymbol{v}_h)\right\rangle_{\partial E}.\end{aligned}\tag{5.3}$$

Collecting equalities (5.2), (5.3) and reusing the interface conditions (2.3b), (2.3c), we further deduce that

$$\begin{aligned}&-(2\nu\mathrm{div}\epsilon(\boldsymbol{u}),\boldsymbol{\Pi}_h^o\boldsymbol{v}_h^{\mathrm{div}})_{\Omega_s} + \langle p_s-p_d,\boldsymbol{v}_h^{\mathrm{div}}\cdot\boldsymbol{n}_s\rangle_\Gamma - a_h(\boldsymbol{u}_I|_{\Omega_s},\boldsymbol{v}_h|_{\Omega_s})\\ &= 2\nu(\epsilon(\boldsymbol{u})-\epsilon_h^w(\boldsymbol{u}_I),\epsilon(\boldsymbol{\Pi}_h^o\boldsymbol{v}_h^{\mathrm{div}}))_{\Omega_s} + \sum_{E\in\mathcal{T}_{h,s}}2\nu\left\langle(\epsilon(\boldsymbol{u})-\epsilon_h^w(\boldsymbol{u}_I))\boldsymbol{n},\mathcal{J}_{\partial E}(\boldsymbol{v}_h)\right\rangle_{\partial E} - 2\nu s_1(\boldsymbol{u}_I,\boldsymbol{v}_h)\\ &\quad - \sum_{E\in\mathcal{T}_{h,s}}\left\langle 2\nu\epsilon(\boldsymbol{u})\boldsymbol{n},(\boldsymbol{v}_h^{\mathrm{div}}\cdot\boldsymbol{n})\boldsymbol{n}+\sum_{j=1}^{d-1}(\boldsymbol{v}_h^t\cdot\boldsymbol{\tau}_j)\boldsymbol{\tau}_j\right\rangle_{\partial E\cap\Gamma} + \langle p_s-p_d,\boldsymbol{v}_h^{\mathrm{div}}\cdot\boldsymbol{n}_s\rangle_\Gamma - \sum_{j=1}^{d-1}\alpha\langle\boldsymbol{u}_I^t\cdot\boldsymbol{\tau}_j,\boldsymbol{v}_h^t\cdot\boldsymbol{\tau}_j\rangle_\Gamma\\ &= \sum_{E\in\mathcal{T}_{h,s}}2\nu\left\langle(\epsilon(\boldsymbol{u})-\epsilon_h^w(\boldsymbol{u}_I))\boldsymbol{n},\mathcal{J}_{\partial E}(\boldsymbol{v}_h)\right\rangle_{\partial E} - 2\nu s_1(\boldsymbol{u}_I,\boldsymbol{v}_h).\end{aligned}\tag{5.4}$$

Therefore, combining equalities (5.1) and (5.4), we obtain the error equation which can be summarized in the following lemma.

Lemma 5.1. *For any $\boldsymbol{v}_h\in\boldsymbol{Z}_h$, we have*

$$\begin{aligned}&a_h(\boldsymbol{u}_h-\boldsymbol{u}_I,\boldsymbol{v}_h)\\ &= (\boldsymbol{f}+2\nu\mathrm{div}\,\epsilon(\boldsymbol{u}),\boldsymbol{\Pi}_h^o\boldsymbol{v}_h^{\mathrm{div}}-\boldsymbol{v}_h^{\mathrm{div}})_{\Omega_s} + \sum_{E\in\mathcal{T}_{h,s}}2\nu\left\langle(\epsilon(\boldsymbol{u})-\epsilon_h^w(\boldsymbol{u}_I))\boldsymbol{n},\mathcal{J}_{\partial E}(\boldsymbol{v}_h)\right\rangle_{\partial E} - 2\nu s_1(\boldsymbol{u}_I,\boldsymbol{v}_h)\\ &\quad + \mathbb{K}^{-1}(\boldsymbol{u}-\boldsymbol{\Pi}_h^o\boldsymbol{u}_I^{\mathrm{div}},\boldsymbol{v}_h^{\mathrm{div}})_{\Omega_d} - \mathbb{K}^{-1}s_2(\boldsymbol{u}_I^{\mathrm{div}},\boldsymbol{v}_h^{\mathrm{div}}).\end{aligned}\tag{5.5}$$

5.2. Error estimates

With the error equation established in Lemma 5.1, we are ready to present error estimates of scheme (4.1).

Theorem 5.2. *Let $(\boldsymbol{u},p)$ be the solution to (2.1)–(2.3) and $(\boldsymbol{u}_h,p_h)\in\boldsymbol{V}_h\times Q_h$ be the solution to (4.1). Furthermore, assume that $\boldsymbol{u}_s\in\boldsymbol{H}^{k+1}(\Omega_s)$, $\boldsymbol{u}_d\in\boldsymbol{H}^k(\Omega_d)$ and $p\in H^k(\Omega)$. Then, the following estimate holds true,*

$$|||\boldsymbol{u}_h-\boldsymbol{u}_I||| + \|p_h-p_I\| \lesssim h^k\left(\nu^{\frac12}\|\boldsymbol{u}\|_{k+1,\Omega_s} + \mathbb{K}^{-\frac12}\|\boldsymbol{u}\|_{k,\Omega_d}\right) + \nu^{-\frac12}h\|\boldsymbol{f}-\boldsymbol{\Pi}_h^o\boldsymbol{f}\|_{\Omega_s}.\tag{5.6}$$

Moreover, we have

$$\|p-p_h\| \lesssim \frac{1}{b_*}\left(\nu^{\frac12}h^k\|\boldsymbol{u}\|_{k+1,\Omega_s} + \mathbb{K}^{-\frac12}h^k\|\boldsymbol{u}\|_{k,\Omega_d} + \nu^{-\frac12}h\|\boldsymbol{f}-\boldsymbol{\Pi}_h^o\boldsymbol{f}\|_{\Omega_s}\right) + h^k\|p\|_{k,\Omega}.\tag{5.7}$$

Proof. Choosing $\boldsymbol{v}_h=\boldsymbol{u}_h-\boldsymbol{u}_I$, using the $\boldsymbol{Z}_h$-coercivity of $a_h(\cdot,\cdot)$ and Lemma 5.1, we get

$$|||\boldsymbol{u}_h-\boldsymbol{u}_I|||^2 \lesssim a_h(\boldsymbol{u}_h-\boldsymbol{u}_I,\boldsymbol{v}_h) \triangleq \mathrm{I}_1+\mathrm{I}_2+\mathrm{I}_3+\mathrm{I}_4+\mathrm{I}_5.$$

We are ready to derive an upper bound for each term I_i, $i = 1, \ldots, 5$. For the first term I_1, a use of the Cauchy–Schwarz inequality and the inequalities (3.8a), (4.3a) yields

$$\begin{aligned}
\mathrm{I}_1 &= \left((\boldsymbol{I} - \boldsymbol{\Pi}_h^o)(\boldsymbol{f} + 2\nu \mathrm{div}\, \epsilon(\boldsymbol{u})), \boldsymbol{\Pi}_h^o \boldsymbol{v}_h^{\mathrm{div}} - \boldsymbol{v}_h^{\mathrm{div}}\right)_{\Omega_s} \\
&\leq \left(\|\boldsymbol{f} - \boldsymbol{\Pi}_h^o \boldsymbol{f}\|_{\Omega_s} + 2\nu \|\mathrm{div}\, \epsilon(\boldsymbol{u}) - \boldsymbol{\Pi}_h^o \mathrm{div}\, \epsilon(\boldsymbol{u})\|_{\Omega_s}\right) \|\boldsymbol{\Pi}_h^o \boldsymbol{v}_h^{\mathrm{div}} - \boldsymbol{v}_h^{\mathrm{div}}\|_{\Omega_s} \\
&\lesssim \left(\|\boldsymbol{f} - \boldsymbol{\Pi}_h^o \boldsymbol{f}\|_{\Omega_s} + \nu h^{k-1} \|\boldsymbol{u}\|_{k+1,\Omega_s}\right) \left(\sum_{E \in \mathcal{T}_{h,s}} h \|\mathcal{J}_{\partial E}^{\boldsymbol{n}}(\boldsymbol{v}_h^{\mathrm{div}})\|_{\partial E}^2\right)^{\frac{1}{2}} \\
&\lesssim \left(\nu^{-\frac{1}{2}} h \|\boldsymbol{f} - \boldsymbol{\Pi}_h^o \boldsymbol{f}\|_{\Omega_s} + \nu^{\frac{1}{2}} h^k \|\boldsymbol{u}\|_{k+1,\Omega_s}\right) |||\boldsymbol{v}_h|||_{\Omega_s}.
\end{aligned} \tag{5.8}$$

The second term I_2 can be bounded by using the Cauchy–Schwarz inequality, the trace inequality and the inequalities (3.8d), (4.3b) in turn, so that we obtain

$$\begin{aligned}
\mathrm{I}_2 &\leq \sum_{E \in \mathcal{T}_{h,s}} 2\nu \|\epsilon(\boldsymbol{u}) - \epsilon_h^w(\boldsymbol{u}_I)\|_{\partial E} \|\mathcal{J}_{\partial E}(\boldsymbol{v}_h)\|_{\partial E} \\
&\lesssim \nu h^k \|\boldsymbol{u}\|_{k+1,\Omega_s} \left(\sum_{E \in \mathcal{T}_{h,s}} h^{-1} \|\boldsymbol{\Pi}_{\partial E} \mathcal{J}_{\partial E}(\boldsymbol{v}_h)\|_{\partial E}^2 + \|\epsilon_h^w(\boldsymbol{v}_h)\|_E^2\right)^{\frac{1}{2}} \\
&\lesssim \nu^{\frac{1}{2}} h^k \|\boldsymbol{u}\|_{k+1,\Omega_s} |||\boldsymbol{v}_h|||_{\Omega_s}.
\end{aligned} \tag{5.9}$$

To get the bound for I_3, by using the Cauchy–Schwarz inequality and the inequality (3.8c), we find

$$\begin{aligned}
\mathrm{I}_3 &= -2\nu \sum_{E \in \mathcal{T}_{h,s}} h^{-1} \left\langle \boldsymbol{\Pi}_{\partial E} \mathcal{J}_{\partial E}(\boldsymbol{u}_I), \boldsymbol{\Pi}_{\partial E} \mathcal{J}_{\partial E}(\boldsymbol{v}_h) \right\rangle_{\partial E} \\
&\lesssim \nu \sum_{E \in \mathcal{T}_{h,s}} h^{-1} \|\boldsymbol{\Pi}_{\partial E} \mathcal{J}_{\partial E}(\boldsymbol{u}_I)\|_{\partial E} \|\boldsymbol{\Pi}_{\partial E} \mathcal{J}_{\partial E}(\boldsymbol{v}_h)\|_{\partial E} \\
&\lesssim \nu \sum_{E \in \mathcal{T}_{h,s}} h^{k-\frac{1}{2}} \|\boldsymbol{u}\|_{k+1,E} \|\boldsymbol{\Pi}_{\partial E} \mathcal{J}_{\partial E}(\boldsymbol{v}_h)\|_{\partial E} \\
&\lesssim \nu^{\frac{1}{2}} h^k \|\boldsymbol{u}\|_{k+1,\Omega_s} |||\boldsymbol{v}_h|||_{\Omega_s}.
\end{aligned} \tag{5.10}$$

Let us now bound I_4 and I_5 together. Taking $\boldsymbol{q} = \boldsymbol{\Pi}_h^o \boldsymbol{v}_h^{\mathrm{div}}$ in the definition (3.3) and using the Cauchy–Schwarz inequality, we have that $\|\boldsymbol{\Pi}_h^o \boldsymbol{v}_h^{\mathrm{div}}\|_{\Omega_d} \leq \|\boldsymbol{v}_h^{\mathrm{div}}\|_{\Omega_d}$. Based on this result, we then have from the inequality (3.8b) that

$$\begin{aligned}
\mathrm{I}_4 + \mathrm{I}_5 &= \mathbb{K}^{-1}(\boldsymbol{u} - \boldsymbol{\Pi}_h^o \boldsymbol{u}_I^{\mathrm{div}}, \boldsymbol{v}_h^{\mathrm{div}})_{\Omega_d} - \mathbb{K}^{-1} s_2(\boldsymbol{u}_I^{\mathrm{div}}, \boldsymbol{v}_h^{\mathrm{div}}) \\
&\lesssim \mathbb{K}^{-1} \|\boldsymbol{u} - \boldsymbol{\Pi}_h^o \boldsymbol{u}_I^{\mathrm{div}}\|_{\Omega_d} \|\boldsymbol{v}_h^{\mathrm{div}}\|_{\Omega_d} + \mathbb{K}^{-1} \|\boldsymbol{u}_I^{\mathrm{div}} - \boldsymbol{\Pi}_h^o \boldsymbol{u}_I^{\mathrm{div}}\|_{\Omega_d} \|\boldsymbol{v}_h^{\mathrm{div}} - \boldsymbol{\Pi}_h^o \boldsymbol{v}_h^{\mathrm{div}}\|_{\Omega_d} \\
&\lesssim \mathbb{K}^{-1} \left(\|\boldsymbol{u} - \boldsymbol{\Pi}_h^o \boldsymbol{u}_I^{\mathrm{div}}\|_{\Omega_d} + \|\boldsymbol{u}_I^{\mathrm{div}} - \boldsymbol{u} + \boldsymbol{u} - \boldsymbol{\Pi}_h^o \boldsymbol{u}_I^{\mathrm{div}}\|_{\Omega_d}\right) \|\boldsymbol{v}_h^{\mathrm{div}}\|_{\Omega_d} \\
&\lesssim \mathbb{K}^{-1} \left(\|\boldsymbol{u} - \boldsymbol{u}_I^{\mathrm{div}}\|_{\Omega_d} + \|\boldsymbol{u} - \boldsymbol{\Pi}_h^o \boldsymbol{u}_I^{\mathrm{div}}\|_{\Omega_d}\right) \|\boldsymbol{v}_h^{\mathrm{div}}\|_{\Omega_d} \\
&\lesssim \mathbb{K}^{-1} h^k \|\boldsymbol{u}\|_{k,\Omega_d} \|\boldsymbol{v}_h^{\mathrm{div}}\|_{\Omega_d} \\
&\lesssim \mathbb{K}^{-\frac{1}{2}} h^k \|\boldsymbol{u}\|_{k,\Omega_d} |||\boldsymbol{v}_h|||_{\Omega_d}.
\end{aligned} \tag{5.11}$$

So that, we have proved that

$$|||\boldsymbol{u}_h - \boldsymbol{u}_I||| \lesssim h^k \left(\nu^{\frac{1}{2}} \|\boldsymbol{u}\|_{k+1,\Omega_s} + \mathbb{K}^{-\frac{1}{2}} \|\boldsymbol{u}\|_{k,\Omega_d}\right) + \nu^{-\frac{1}{2}} h \|\boldsymbol{f} - \boldsymbol{\Pi}_h^o \boldsymbol{f}\|_{\Omega_s}.$$

In order to conclude, it remains to bound the term $p_I - p_h$. We observe from Lemma 4.8 that there exists $\boldsymbol{v}_h = (\boldsymbol{v}_h^{\mathrm{div}}, \boldsymbol{v}_h^t) \in \boldsymbol{V}_h$ such that

$$\mathrm{div}\, \boldsymbol{v}_h^{\mathrm{div}} = p_I - p_h \text{ and } b_* |||\boldsymbol{v}_h||| \lesssim \|p_I - p_h\|.$$

Then, we derive that

$$\begin{aligned}\|p_I - p_h\|^2 &= (p_I - p_h, \operatorname{div} \boldsymbol{v}_h^{\mathrm{div}}) \\ &= (p_I, \operatorname{div} \boldsymbol{v}_h^{\mathrm{div}}) - (p_h, \operatorname{div} \boldsymbol{v}_h^{\mathrm{div}}) \\ &= (p_I, \operatorname{div} \boldsymbol{v}_h^{\mathrm{div}}) + (\boldsymbol{f}, \boldsymbol{\Pi}_h^o \boldsymbol{v}_h^{\mathrm{div}})_{\Omega_s} - a_h(\boldsymbol{u}_h, \boldsymbol{v}_h) \\ &= (p_I, \operatorname{div} \boldsymbol{v}_h^{\mathrm{div}}) + (\boldsymbol{f}, \boldsymbol{\Pi}_h^o \boldsymbol{v}_h^{\mathrm{div}} - \boldsymbol{v}_h^{\mathrm{div}})_{\Omega_s} + (-2\nu \operatorname{div} \epsilon(\boldsymbol{u}) + \nabla p, \boldsymbol{v}_h^{\mathrm{div}})_{\Omega_s} - a_h(\boldsymbol{u}_h, \boldsymbol{v}_h) \\ &+ (\nabla p, \boldsymbol{v}_h^{\mathrm{div}})_{\Omega_d} - (\nabla p, \boldsymbol{v}_h^{\mathrm{div}})_{\Omega_d} \\ &= (p_I - p, \operatorname{div} \boldsymbol{v}_h^{\mathrm{div}}) + (\boldsymbol{f}, \boldsymbol{\Pi}_h^o \boldsymbol{v}_h^{\mathrm{div}} - \boldsymbol{v}_h^{\mathrm{div}})_{\Omega_s} + (-2\nu \operatorname{div} \epsilon(\boldsymbol{u}), \boldsymbol{v}_h^{\mathrm{div}})_{\Omega_s} - a_h(\boldsymbol{u}_h, \boldsymbol{v}_h) \\ &+ \langle p_s - p_d, \boldsymbol{v}_h^{\mathrm{div}} \cdot \boldsymbol{n}_s \rangle_\Gamma + \mathbb{K}^{-1}(\boldsymbol{u}, \boldsymbol{v}_h^{\mathrm{div}})_{\Omega_d}.\end{aligned} \tag{5.12}$$

Using the fact $(p_I - p, \operatorname{div} \boldsymbol{v}_h^{\mathrm{div}}) = 0$, the deduction of (5.1)–(5.11) and the continuous property (4.7a), we obtain

$$\begin{aligned}\|p_I - p_h\|^2 &= (\boldsymbol{f}, \boldsymbol{\Pi}_h^o \boldsymbol{v}_h^{\mathrm{div}} - \boldsymbol{v}_h^{\mathrm{div}})_{\Omega_s} + (-2\nu \operatorname{div} \epsilon(\boldsymbol{u}), \boldsymbol{v}_h^{\mathrm{div}})_{\Omega_s} \\ &+ \langle p_s - p_d, \boldsymbol{v}_h^{\mathrm{div}} \cdot \boldsymbol{n}_s \rangle_\Gamma + \mathbb{K}^{-1}(\boldsymbol{u}, \boldsymbol{v}_h^{\mathrm{div}})_{\Omega_d} - a_h(\boldsymbol{u}_I, \boldsymbol{v}_h) + a_h(\boldsymbol{u}_I - \boldsymbol{u}_h, \boldsymbol{v}_h) \\ &\lesssim \left(\nu^{\frac{1}{2}} h^k \|\boldsymbol{u}\|_{k+1,\Omega_s} + \mathbb{K}^{-\frac{1}{2}} h^k \|\boldsymbol{u}\|_{k,\Omega_d} + \nu^{-\frac{1}{2}} h \|\boldsymbol{f} - \boldsymbol{\Pi}_h^o \boldsymbol{f}\|_{\Omega_s} \right) |||\boldsymbol{v}_h|||.\end{aligned} \tag{5.13}$$

Combining the above bounds gives the first inequality (5.6). With the triangle inequality, this further leads to

$$\|p - p_h\| \le \|p - p_I\| + \|p_I - p_h\| \lesssim h^k \|p\|_{k,\Omega} + \|p_I - p_h\|. \tag{5.14}$$

The second inequality (5.7) is obtained by combining the above two bounds. The proof is completed. □

6. Numerical experiments

In this section, we shall present some two-dimensional numerical experiments to confirm our theoretical results. As mentioned before, we can only compute three terms for the function $\boldsymbol{u}$ on an element $E \in \mathcal{T}_h$, i.e., $\boldsymbol{u} \cdot \boldsymbol{n}$ on ∂E and $\operatorname{div} \boldsymbol{u}$, $\operatorname{rot} \boldsymbol{u}$ inside E. Therefore, the error $\boldsymbol{u} - \boldsymbol{u}_h$ is not computable. Instead, we compute three errors, respectively, $\boldsymbol{e}_{\boldsymbol{u}} := \boldsymbol{u}_h - \boldsymbol{u}_I$, $e_p := P_h p - p_h$, $\tilde{e}_p = p - p_h$. We will present the errors $\|\boldsymbol{e}_{\boldsymbol{u}}\|_{0,h}$, $|||\boldsymbol{e}_{\boldsymbol{u}}|||$, $\|e_p\|$ and $\|\tilde{e}_p\|$ by using the lowest order element ($k = 1$), where the norm $\|\cdot\|_{0,h}$ is defined as

$$\|\boldsymbol{e}_{\boldsymbol{u}}\|_{0,h}^2 := \sum_{E \in \mathcal{T}_h} \|\boldsymbol{\Pi}_E^o \boldsymbol{e}_{\boldsymbol{u}}^{\mathrm{div}}\|_E^2 + \sum_{E \in \mathcal{T}_{h,s}} h \|\boldsymbol{\Pi}_{\partial E} \mathcal{J}_{\partial E}(\boldsymbol{e}_{\boldsymbol{u}})\|_{\partial E}^2 + \sum_{E \in \mathcal{T}_{h,d}} \mathcal{D}^E((I - \boldsymbol{\Pi}_h^o)\boldsymbol{e}_{\boldsymbol{u}}^{\mathrm{div}}, (I - \boldsymbol{\Pi}_h^o)\boldsymbol{e}_{\boldsymbol{u}}^{\mathrm{div}}).$$

Note that this norm can be computed using the matrices assembled from the degrees of freedom and the discrete scheme (4.1). In order to demonstrate that the method produces a divergence free velocity, the quantity $\|\operatorname{div} \boldsymbol{u}_h^{\mathrm{div}} - \chi_{\Omega_d} g_I\|$ denoted by δ will be computed, where χ_{Ω_d} denotes the characteristic function of the subdomain Ω_d and $g_I = P_h g$.

6.1. Example 1

Let the domain be $\Omega = (0, 1) \times (0, 2)$, where $\Omega_s = (0, 1) \times (1, 2)$ and $\Omega_d = (0, 1) \times (0, 1)$. Take the parameters as $\nu = 1$, $\alpha = 1$ and $\mathbb{K} = \mathbb{I}$, where $\mathbb{I}$ is the identity matrix. We test eight types of meshes, as shown in Fig. 3, that is, uniform triangular mesh $\mathcal{T}^1$, uniform rectangular mesh $\mathcal{T}^2$, quadrilateral mesh $\mathcal{T}^3$ by perturbing the interior nodes of $\mathcal{T}^2$ with a parameter 0.25 (see [50] for details), polygonal mesh $\mathcal{T}^4$ generated by the dual of the triangle mesh $\mathcal{T}^1$, distorted polygonal mesh $\mathcal{T}^5$, centroid Voronoi Tessellation (CVT) mesh $\mathcal{T}^6$ generated by PolyMesher package [51], non-convex mesh $\mathcal{T}^7$ and hybrid mesh $\mathcal{T}^8$ by directly cutting the triangular mesh across the interface. All types of meshes are aligned to the interface. The exact solution is set to be

$$\boldsymbol{u}_s = \begin{pmatrix} -\cos(\pi x)\sin(\pi y) \\ \sin(\pi x)\cos(\pi y) \end{pmatrix}, \quad \boldsymbol{u}_d = \begin{pmatrix} -\pi y \cos(\pi x) \\ -\sin(\pi x) \end{pmatrix},$$
$$p_s = \sin(\pi x), \quad p_d = y \sin(\pi x).$$

It is easy to check that the given exact solution satisfies the interface conditions (2.3). Note that the normal velocity is continuous, but the tangential velocity is discontinuous across the interface Γ. In addition, the pressure is continuous

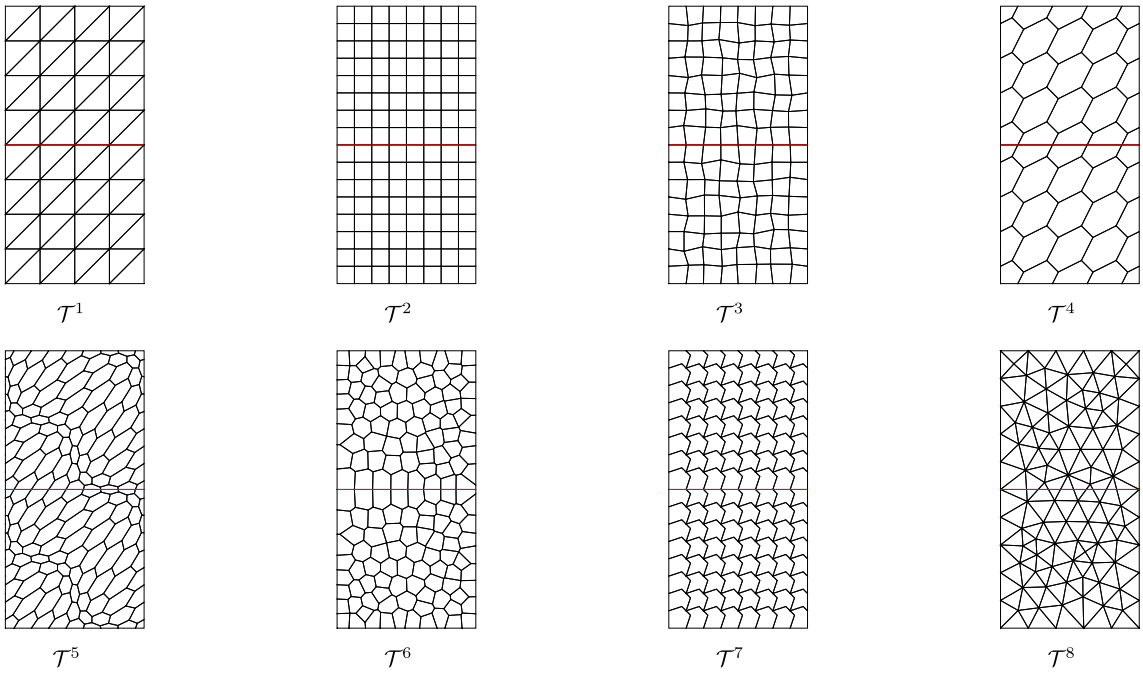

Fig. 3. Illustrations of meshes. The interface Γ is colored in red. (For interpretation of the references to color in this figure legend, the reader is referred to the web version of this article.)

Table 1
The errors for a series of the uniform triangular meshes $\mathcal{T}^1$ (upper) and uniform rectangular meshes $\mathcal{T}^2$ (below) for Example 1.

♯Dof	$\|\boldsymbol{e_u}\|_{0,h}$	r	$\|\!\|\!\|\boldsymbol{e_u}\|\!\|\!\|$	r	$\|e_p\|$	r	$\|\tilde{e}_p\|$	r	δ
108	2.4179e−01	–	1.3747e+00	–	1.3158e+00	–	1.3503e+00	–	6.6242e−16
400	4.0579e−02	5.96	5.9916e−01	2.29	6.4716e−01	2.03	6.6558e−01	2.03	1.1588e−15
1536	7.3584e−03	5.51	2.7503e−01	2.18	3.1017e−01	2.09	3.1988e−01	2.08	8.4911e−15
6016	1.5444e−03	4.76	1.3226e−01	2.08	1.5015e−01	2.07	1.5518e−01	2.06	5.163e−15
23808	3.6397e−04	4.24	6.5290e−02	2.03	7.3705e−02	2.04	7.6266e−02	2.03	4.5393e−14
94720	8.9523e−05	4.07	3.2527e−02	2.01	3.6546e−02	2.02	3.7836e−02	2.02	4.7371e−13
377856	2.2286e−05	4.02	1.6248e−02	2	1.8212e−02	2.01	1.8860e−02	2.01	2.2231e−12
256	4.2869e−02	–	4.8691e−01	–	2.4169e−01	–	3.0734e−01	–	7.1572e−16
960	6.3121e−03	6.79	1.7507e−01	2.78	1.0863e−01	2.22	1.4480e−01	2.12	9.4663e−15
3712	9.1972e−04	6.86	6.9836e−02	2.51	4.5237e−02	2.4	6.5937e−02	2.2	2.4446e−14
14592	1.5425e−04	5.96	3.1790e−02	2.2	1.5633e−02	2.89	2.8642e−02	2.3	3.9544e−14
57856	3.1658e−05	4.87	1.5443e−02	2.06	4.9643e−03	3.15	1.2987e−02	2.21	6.0122e−13
230400	7.4051e−06	4.28	7.6617e−03	2.02	1.5407e−03	3.22	6.1953e−03	2.1	1.0154e−12

on Γ. The error profiles and the quantity δ are listed in Tables 1–4, where r denotes the corresponding ratios of the errors on two successive meshes. We observe that $|\!|\!|\boldsymbol{e_u}|\!|\!|$, $\|e_p\|$ and $\|\tilde{e}_p\|$ converge in the order of $O(h)$, in accordance with Theorem 5.2. Beyond that, a superconvergence effect for $\|e_p\|$ is also observed on meshes $\mathcal{T}^2$, $\mathcal{T}^4$, $\mathcal{T}^5$ and $\mathcal{T}^7$ (see columns 6–7 in Tables 1–4). In addition, it is observed that the error $\|\boldsymbol{e_u}\|_{0,h}$ for the velocity is of the order $O(h^2)$. We also find that the quantity δ is machine zero for all meshes.

6.2. Example 2

In this test, the domain is $\Omega = (0,1)\times(-1,1)$, where $\Omega_s = (0,1)\times(0,1)$ and $\Omega_d = (0,1)\times(-1,0)$. All parameters retain unchanged as set in Example 1 except that $\mathbb{K} = \beta\mathbb{I}$, β is a positive constant determined later. The

Table 2
The errors for a series of quadrilateral meshes $\mathcal{T}^3$ (upper) and polygonal meshes $\mathcal{T}^4$ (below) for Example 1.

♯Dof	$\|\boldsymbol{e_u}\|_{0,h}$	r	$\|\boldsymbol{e_u}\|$	r	$\|e_p\|$	r	$\|\tilde{e}_p\|$	r	δ
256	5.6585e−02	–	5.9050e−01	–	2.8526e−01	–	3.4445e−01	–	3.1043e−15
960	9.8395e−03	5.75	2.3773e−01	2.48	1.2854e−01	2.22	1.6066e−01	2.14	2.6235e−15
3712	3.0387e−03	3.24	1.4201e−01	1.67	6.9536e−02	1.85	8.4884e−02	1.89	3.9218e−14
14592	7.4209e−04	4.09	7.1197e−02	1.99	2.4108e−02	2.88	3.4253e−02	2.48	7.0002e−15
57856	1.8701e−04	3.97	3.4774e−02	2.05	8.9992e−03	2.68	1.5158e−02	2.26	2.7818e−13
230400	4.6761e−05	4	1.7282e−02	2.01	3.7744e−03	2.38	7.1700e−03	2.11	2.9581e−13
188	1.0426e−01	–	1.0879e+00	–	7.6995e−01	–	7.9928e−01	–	1.307e−15
524	6.8255e−02	1.53	9.9104e−01	1.1	1.1014e+00	0.699	1.1127e+00	0.718	3.1416e−15
1652	1.9286e−02	3.54	6.7429e−01	1.47	6.6446e−01	1.66	6.7061e−01	1.66	2.6424e−15
5732	4.5597e−03	4.23	3.8811e−01	1.74	2.5188e−01	2.64	2.5642e−01	2.62	5.5409e−14
21188	1.0455e−03	4.36	2.0637e−01	1.88	7.9958e−02	3.15	8.3676e−02	3.06	2.6967e−14
81284	2.4712e−04	4.23	1.0606e−01	1.95	2.4323e−02	3.29	2.7344e−02	3.06	1.6379e−13
318212	6.0017e−05	4.12	5.3712e−02	1.97	7.5248e−03	3.23	9.8049e−03	2.79	3.2573e−12

Table 3
The errors for a series of the distorted polygonal meshes $\mathcal{T}^5$ (upper) and CVT meshes $\mathcal{T}^6$ (below) for Example 1.

♯Dof	$\|\boldsymbol{e_u}\|_{0,h}$	r	$\|\boldsymbol{e_u}\|$	r	$\|e_p\|$	r	$\|\tilde{e}_p\|$	r	δ
188	1.2543e−01	–	1.0766e+00	–	8.0609e−01	–	8.3713e−01	–	1.0688e−15
524	7.9650e−02	1.57	1.0387e+00	1.04	9.8332e−01	0.82	9.9781e−01	0.839	4.0252e−15
1652	3.6352e−02	2.19	8.1766e−01	1.27	9.8203e−01	1	9.8752e−01	1.01	2.534e−14
5732	1.1961e−02	3.04	5.2069e−01	1.57	5.1413e−01	1.91	5.1724e−01	1.91	6.1254e−14
21188	3.3174e−03	3.61	2.9046e−01	1.79	1.7536e−01	2.93	1.7780e−01	2.91	1.427e−13
81284	8.6528e−04	3.83	1.5212e−01	1.91	5.2219e−02	3.36	5.4304e−02	3.27	1.9211e−13
318212	2.2168e−04	3.9	7.7596e−02	1.96	1.5706e−02	3.32	1.7408e−02	3.12	4.4855e−12
370	5.2713e−02	–	7.7433e−01	–	4.7835e−01	–	5.0612e−01	–	4.8967e−14
1484	1.1695e−02	4.51	4.6202e−01	1.68	2.6807e−01	1.78	2.8142e−01	1.8	8.6134e−15
5636	2.5037e−03	4.67	2.6874e−01	1.72	9.8175e−02	2.73	1.0774e−01	2.61	3.9267e−15
22796	5.8092e−04	4.31	1.3947e−01	1.93	3.2687e−02	3	3.9389e−02	2.74	3.5223e−14
93369	1.3961e−04	4.16	7.0702e−02	1.97	1.8291e−02	1.79	2.1324e−02	1.85	2.1709e−13

Table 4
The errors for a series of the non-convex meshes $\mathcal{T}^7$ (upper) and the hybrid meshes $\mathcal{T}^8$ (below) for Example 1.

♯Dof	$\|\boldsymbol{e_u}\|_{0,h}$	r	$\|\boldsymbol{e_u}\|$	r	$\|e_p\|$	r	$\|\tilde{e}_p\|$	r	δ
128	2.7451e−01	–	1.3361e+00	–	4.1707e−01	–	5.5428e−01	–	8.2942e−16
448	7.9067e−02	3.47	1.0331e+00	1.29	6.6463e−01	0.628	6.9290e−01	0.8	2.5806e−15
1664	1.9670e−02	4.02	6.8398e−01	1.51	4.8134e−01	1.38	4.9143e−01	1.41	2.53e−15
6400	4.2670e−03	4.61	3.8798e−01	1.76	2.1580e−01	2.23	2.2141e−01	2.22	1.2507e−14
25088	9.7599e−04	4.37	2.0518e−01	1.89	7.5727e−02	2.85	7.9674e−02	2.78	4.9222e−14
99328	2.3567e−04	4.14	1.0524e−01	1.95	2.4033e−02	3.15	2.7033e−02	2.95	1.9963e−13
395264	5.8192e−05	4.05	5.3257e−02	1.98	7.4619e−03	3.22	9.6934e−03	2.79	1.5299e−12
1096	2.0144e−02	–	4.1673e−01	–	8.9366e−01	–	8.9844e−01	–	2.7579e−14
4210	5.3477e−03	3.77	2.2782e−01	1.83	4.7146e−01	1.9	4.7374e−01	1.9	3.7243e−14
16291	1.4033e−03	3.81	1.2003e−01	1.9	2.1472e−01	2.2	2.1598e−01	2.19	1.4737e−13
64135	3.6298e−04	3.87	6.1438e−02	1.95	9.0451e−02	2.37	9.1195e−02	2.37	1.0135e−12
254446	9.1803e−05	3.95	3.0970e−02	1.98	4.1179e−02	2.2	4.1587e−02	2.19	1.8494e−13

exact solution is given as

$$\boldsymbol{u}_s = \begin{pmatrix} \dfrac{1}{\pi}\cos(x)\sin(2\pi y) \\ \left(-2 + \dfrac{1}{\pi^2}\sin^2(\pi y)\right)\sin(x) \end{pmatrix},$$

Table 5
The errors for a series of the uniform triangular meshes $\mathcal{T}^1$ (upper) and uniform rectangular meshes $\mathcal{T}^2$ (below) for Example 2.

♯Dof	$\|\boldsymbol{e_u}\|_{0,h}$	r	$\|\boldsymbol{e_u}\|$	r	$\|e_p\|$	r	$\|\tilde{e}_p\|$	r	δ
108	1.2749e−01	–	7.9976e−01	–	5.4454e−01	–	6.2954e−01	–	1.2009e−15
400	4.3483e−02	2.93	5.9676e−01	1.34	3.5578e−01	1.53	3.8950e−01	1.62	1.5454e−15
1536	1.3647e−02	3.19	3.5061e−01	1.7	1.5700e−01	2.27	1.7591e−01	2.21	4.9151e−15
6016	3.7629e−03	3.63	1.8593e−01	1.89	5.8587e−02	2.68	7.0755e−02	2.49	5.7292e−15
23808	9.7365e−04	3.86	9.4615e−02	1.97	2.3113e−02	2.53	3.0458e−02	2.32	1.6892e−14
94720	2.4586e−04	3.96	4.7531e−02	1.99	1.0396e−02	2.22	1.4369e−02	2.12	2.9838e−14
377856	6.1631e−05	3.99	2.3794e−02	2	5.0308e−03	2.07	7.0643e−03	2.03	6.959e−14
256	4.0816e−02	–	6.4836e−01	–	4.0329e−01	–	4.4747e−01	–	7.5094e−16
960	1.2746e−02	3.2	3.9053e−01	1.66	1.6135e−01	2.5	1.8833e−01	2.38	2.5107e−15
3712	3.3740e−03	3.78	2.0724e−01	1.88	4.8548e−02	3.32	6.8684e−02	2.74	4.5074e−15
14592	8.5512e−04	3.95	1.0532e−01	1.97	1.2903e−02	3.76	2.7509e−02	2.5	6.9276e−15
57856	2.1473e−04	3.98	5.2882e−02	1.99	3.2828e−03	3.93	1.2584e−02	2.19	2.9961e−14
230400	5.3776e−05	3.99	2.6469e−02	2	8.2477e−04	3.98	6.1298e−03	2.05	3.4015e−14

Table 6
The errors for a series of quadrilateral meshes $\mathcal{T}^3$ (upper) and polygonal meshes $\mathcal{T}^4$ (below) for Example 2.

♯Dof	$\|\boldsymbol{e_u}\|_{0,h}$	r	$\|\boldsymbol{e_u}\|$	r	$\|e_p\|$	r	$\|\tilde{e}_p\|$	r	δ
256	4.1183e−02	–	6.4991e−01	–	4.3626e−01	–	4.7830e−01	–	1.0468e−15
960	1.4197e−02	2.9	3.9982e−01	1.63	1.6517e−01	2.64	1.9233e−01	2.49	2.2929e−15
3712	3.6576e−03	3.88	2.1087e−01	1.9	5.5205e−02	2.99	7.3930e−02	2.6	5.0121e−15
14592	9.5297e−04	3.84	1.0749e−01	1.96	1.8176e−02	3.04	3.0628e−02	2.41	1.6484e−14
57856	2.3922e−04	3.98	5.4035e−02	1.99	7.0881e−03	2.56	1.4230e−02	2.15	2.7534e−14
230400	5.9914e−05	3.99	2.7028e−02	2	3.2900e−03	2.15	6.9914e−03	2.04	4.2802e−14
188	8.9911e−02	–	7.1150e−01	–	3.4776e−01	–	4.6596e−01	–	1.0507e−15
524	4.6706e−02	1.93	5.8148e−01	1.22	3.1724e−01	1.1	3.6479e−01	1.28	1.6686e−15
1652	1.5372e−02	3.04	3.8038e−01	1.53	1.5255e−01	2.08	1.8037e−01	2.02	2.8797e−15
5732	4.2929e−03	3.58	2.0994e−01	1.81	5.1165e−02	2.98	7.1312e−02	2.53	4.5268e−15
21188	1.1383e−03	3.77	1.0853e−01	1.93	1.4915e−02	3.43	2.9304e−02	2.43	1.7115e−14
81284	2.9406e−04	3.87	5.4887e−02	1.98	4.1943e−03	3.56	1.3383e−02	2.19	2.6052e−14
318212	7.4793e−05	3.93	2.7559e−02	1.99	1.2039e−03	3.48	6.4911e−03	2.06	5.1762e−14

$$p_s = \frac{1}{\beta}\left((e^y + e^{-y})\sin(x) - (1-\cos(1))(e^1 - e^{-1})\right),$$
$$\boldsymbol{u}_d = \begin{pmatrix} -\cos(x)(e^y - e^{-y}) \\ -\sin(x)(e^y + e^{-y}) \end{pmatrix},$$
$$p_d = \frac{1}{\beta}\left((e^y - e^{-y})\sin(x) - (1-\cos(1))(2 - e^1 - e^{-1})\right).$$

On one hand, we remark that the above exact solution does not satisfy the second interface condition (2.3b). A nonhomogeneous term η is included, i.e.,

$$-2\nu\epsilon(\boldsymbol{u}_s)\boldsymbol{n}_s \cdot \boldsymbol{n}_s + p_s = p_d + \eta,$$

where η is a given function on Γ according to the exact solution. The variational form (4.1) after modification only adds one term $\langle -\eta, \boldsymbol{v}_h^{\mathrm{div}} \cdot \boldsymbol{n}_s \rangle_\Gamma$ to the right-hand side of Eq. (4.1a). On the other hand, we see that the normal velocity is continuous, while the tangential velocity is discontinuous, and the pressure is discontinuous on Γ. We first take β as 1, which makes the scale of the pressure remains at about 1. The error results and the quantity δ are listed in Tables 5–8, respectively. The numerical results indicate that the convergence rates predicted by Theorem 5.2 are achieved for corresponding solutions and the quantity δ is close to zero.

To verify the robustness of our method with respect to the pressure, we now take $\beta = 10^{-4}$. It is easy to observe that the scale of the pressure is now around 10^4. The errors and the quantity δ are listed in Table 9. It is observed that the ratios for all errors are still optimal. Although the larger pressure scale increases the error $\|\tilde{e}_p\|$, both the $\boldsymbol{L}^2$ and

Table 7
The errors for a series of the distorted polygonal meshes $\mathcal{T}^5$ (upper) and CVT meshes $\mathcal{T}^6$ (below) for Example 2.

♯Dof	$\|\boldsymbol{e_u}\|_{0,h}$	r	$\|\boldsymbol{e_u}\|$	r	$\|e_p\|$	r	$\|\tilde{e}_p\|$	r	δ
188	1.0950e−01	–	7.3245e−01	–	3.9547e−01	–	5.1838e−01	–	1.3046e−15
524	6.7280e−02	1.63	6.6711e−01	1.1	4.2700e−01	0.926	4.7268e−01	1.1	2.4941e−15
1652	3.3775e−02	1.99	5.0655e−01	1.32	2.7503e−01	1.55	2.9792e−01	1.59	3.0501e−15
5732	1.1938e−02	2.83	3.1206e−01	1.62	1.1794e−01	2.33	1.3245e−01	2.25	8.6151e−15
21188	3.4544e−03	3.46	1.6946e−01	1.84	3.8805e−02	3.04	4.9536e−02	2.67	9.8694e−15
81284	9.1594e−04	3.77	8.7135e−02	1.94	1.1016e−02	3.52	1.9047e−02	2.6	3.2278e−14
318212	2.3465e−04	3.9	4.3961e−02	1.98	2.9411e−03	3.75	8.3379e−03	2.28	5.7592e−14
370	3.1870e−02	–	5.4888e−01	–	2.7228e−01	–	3.2535e−01	–	4.2154e−11
1484	9.1070e−03	3.5	3.1733e−01	1.73	1.0616e−01	2.56	1.3651e−01	2.38	8.6522e−13
5636	2.1837e−03	4.17	1.5737e−01	2.02	2.9744e−02	3.57	5.4166e−02	2.52	7.1239e−15
22672	5.6818e−04	3.84	7.9993e−02	1.97	8.3703e−03	3.55	2.3615e−02	2.29	1.0342e−14
94658	1.3612e−04	4.17	3.9095e−02	2.05	2.8410e−03	2.95	1.1206e−02	2.11	3.1267e−14

Table 8
The errors for a series of the non-convex meshes $\mathcal{T}^7$ (upper) and the hybrid meshes $\mathcal{T}^8$ (below) for Example 2.

♯Dof	$\|\boldsymbol{e_u}\|_{0,h}$	r	$\|\boldsymbol{e_u}\|$	r	$\|e_p\|$	r	$\|\tilde{e}_p\|$	r	δ
128	1.3256e−01	–	8.5599e−01	–	5.2379e−01	–	6.6397e−01	–	4.7225e−16
448	5.2154e−02	2.54	6.9144e−01	1.24	3.8121e−01	1.37	4.3218e−01	1.54	1.4889e−15
1664	1.6039e−02	3.25	4.1465e−01	1.67	1.6393e−01	2.33	1.9263e−01	2.24	1.7918e−15
6400	4.2120e−03	3.81	2.2135e−01	1.87	5.3370e−02	3.07	7.3372e−02	2.63	4.2946e−15
25088	1.0621e−03	3.97	1.1309e−01	1.96	1.5116e−02	3.53	2.9310e−02	2.5	1.0793e−14
99328	2.6642e−04	3.99	5.6937e−02	1.99	4.0686e−03	3.72	1.3183e−02	2.22	2.0023e−14
395264	6.6752e−05	3.99	2.8536e−02	2	1.0966e−03	3.71	6.3606e−03	2.07	4.3324e−14
1096	1.3864e−02	–	2.9912e−01	–	2.1347e−01	–	2.3372e−01	–	2.7127e−15
4210	3.9254e−03	3.53	1.6429e−01	1.82	9.3744e−02	2.28	1.0518e−01	2.22	6.9942e−15
16291	1.0531e−03	3.73	8.5612e−02	1.92	4.0280e−02	2.33	4.6820e−02	2.25	1.5956e−14
64135	2.7138e−04	3.88	4.3451e−02	1.97	1.8389e−02	2.19	2.1925e−02	2.14	2.1227e−14
254446	6.8523e−05	3.96	2.1826e−02	1.99	8.8610e−03	2.08	1.0685e−02	2.05	4.6299e−14

$\boldsymbol{H}^1$ errors for the velocity have little change compared with those in Tables 5–8. These results agree with Theorem 5.2. The results for the case of $\beta = 10^4$ are similar and thus not provided here. The quantity δ is not affected and keeps be machine zero.

6.3. Example 3

We now present a numerical experiment to verify the robustness of mass conservation with respect to the permeability of the porous medium. This experiment has been conducted in [18]. Let the computational domain be $\Omega = (0, 2) \times (0, 2)$, where $\Omega_s = (0, 1) \times (0, 2)$ and $\Omega_d = (1, 2) \times (0, 2)$. In the domain of Stokes flow, we take a quadratic inflow profile $\boldsymbol{u}_s = (y(2 - y), 0)$ on the left and no-slip conditions $\boldsymbol{u}_s = \boldsymbol{0}$ on the top and bottom. For the Darcy part, slip conditions $\boldsymbol{u}_d = \boldsymbol{0}$ are imposed on the top and bottom, while the Dirichlet condition $p_d = 0$ is imposed on the right. The data on the right-hand side are chosen as $\boldsymbol{f} = \boldsymbol{0}$ and $g = 0$. Choose $\nu = 1$, $\alpha = \frac{0.1}{\sqrt{\beta}}$ and the parameter β ($\mathbb{K} = \beta\mathbb{I}$) varies from 10^{-6} to 10^{-8}. Three types of meshes are used, respectively, $\mathcal{T}^1$, $\mathcal{T}^3$ and $\mathcal{T}^8$. Fig. 4 shows the hybrid mesh $\mathcal{T}^8$ which is aligned to the interface. A simple integral tells that the incoming flux on the left of the whole domain is $\frac{4}{3}$. The results of the mass difference between the inflow and outflow side of the domain are displayed in Table 10. We observe that the mass flux error is close to the computational accuracy. This result is better than that of Ref. [18] in which the minimum of the mass flux errors on the triangular meshes is $5.1e - 11$. In fact, we have also obtained similar results for other types of meshes and thus do not report them here. Table 11 shows the results of the quantity δ for different $\mathbb{K}$ and different meshes. It is observed that the quantity δ is of machine precision in all cases. Therefore, we claim that the weak virtual element method retains the mass conservation strongly.

Table 9
The errors for a series of meshes for Example 2 with $\beta = 10^{-4}$.

	♯Dof	$\|\boldsymbol{e_u}\|_{0,h}$	r	$\|\boldsymbol{e_u}\|$	r	$\|e_p\|$	r	$\|\tilde{e}_p\|$	r	δ
	23808	8.5482e−04	–	9.4772e−02	–	2.4144e−02	–	1.9837e+02	–	1.5024e−14
$\mathcal{T}^1$	94720	2.1721e−04	3.94	4.7542e−02	1.99	1.0533e−02	2.29	9.9189e+01	2	3.094e−14
	377856	5.4541e−05	3.98	2.3795e−02	2	5.0483e−03	2.09	4.9595e+01	2	5.7066e−14
	14592	7.7140e−04	–	1.0532e−01	–	1.3319e−02	–	2.4295e+02	–	9.4927e−15
$\mathcal{T}^2$	57856	1.9318e−04	3.99	5.2880e−02	1.99	3.3966e−03	3.92	1.2148e+02	2	1.4993e−14
	230400	4.8312e−05	4	2.6469e−02	2	8.5370e−04	3.98	6.0741e+01	2	3.431e−14
	14592	8.6371e−04	–	1.0746e−01	–	1.8944e−02	–	2.4645e+02	–	1.419e−14
$\mathcal{T}^3$	57856	2.1885e−04	3.95	5.4030e−02	1.99	7.2213e−03	2.62	1.2336e+02	2	2.0526e−14
	230400	5.4721e−05	4	2.7049e−02	2	3.2883e−03	2.2	6.1698e+01	2	5.8648e−14
	21188	9.5310e−04	–	1.1092e−01	–	1.6394e−02	–	2.5224e+02	–	1.5782e−14
$\mathcal{T}^4$	81284	2.5120e−04	3.79	5.5141e−02	2.01	4.5586e−03	3.6	1.2709e+02	1.98	2.3182e−14
	318212	6.4339e−05	3.9	2.7589e−02	2	1.2909e−03	3.53	6.3785e+01	1.99	3.7964e−14
	21188	2.6756e−03	–	1.7095e−01	–	4.7289e−02	–	3.0788e+02	–	1.1747e−14
$\mathcal{T}^5$	81284	6.7689e−04	3.95	8.7185e−02	1.96	1.3312e−02	3.55	1.5537e+02	1.98	3.5381e−14
	318212	1.7205e−04	3.93	4.3965e−02	1.98	3.5323e−03	3.77	7.8020e+01	1.99	5.9555e−14
	5636	2.1554e−03	–	1.8691e−01	–	3.2500e−02	–	4.5268e+02	–	7.3145e−15
$\mathcal{T}^6$	22672	5.0818e−04	4.24	8.1593e−02	2.29	8.5751e−03	3.79	2.2082e+02	2.05	8.6933e−15
	94658	1.2247e−04	4.15	3.9245e−02	2.08	2.8791e−03	2.98	1.0840e+02	2.04	3.6235e−14
	25088	9.7677e−04	–	1.1492e−01	–	1.5504e−02	–	2.5112e+02	–	1.1164e−14
$\mathcal{T}^7$	99328	2.4525e−04	3.98	5.7041e−02	2.01	4.1961e−03	3.69	1.2539e+02	2	1.6062e−14
	395264	6.1493e−05	3.99	2.8545e−02	2	1.1299e−03	3.71	6.2653e+01	2	2.7851e−14
	16291	1.0158e−03	–	8.7386e−02	–	4.0783e−02	–	2.3867e+02	–	1.211e−14
$\mathcal{T}^8$	64135	2.5899e−04	3.92	4.3606e−02	2	1.8472e−02	2.21	1.1939e+02	2	2.7506e−14
	254446	6.5459e−05	3.96	2.1843e−02	2	8.8735e−03	2.08	5.9716e+01	2	4.3081e−14

Table 10
Mass difference between the inflow and outflow sides of the domain for Example 3.

$\mathcal{T}^1$			$\mathcal{T}^3$			$\mathcal{T}^8$		
♯Dof	$\mathbb{K} = 10^{-6}\mathbb{I}$	$\mathbb{K} = 10^{-8}\mathbb{I}$	♯Dof	$\mathbb{K} = 10^{-6}\mathbb{I}$	$\mathbb{K} = 10^{-8}\mathbb{I}$	♯Dof	$\mathbb{K} = 10^{-6}\mathbb{I}$	$\mathbb{K} = 10^{-8}\mathbb{I}$
232	2.2204e−16	2.2204e−16	152	2.2204e−16	4.4409e−16	405	2.2204e−16	0
880	2.2204e−16	4.4409e−16	560	0	0	1533	0	0
3424	2.2204e−16	0	2144	2.2204e−16	0	6089	2.2204e−16	0

Table 11
The quantity δ for Example 3.

$\mathcal{T}^1$			$\mathcal{T}^3$			$\mathcal{T}^8$		
♯Dof	$\mathbb{K} = 10^{-6}\mathbb{I}$	$\mathbb{K} = 10^{-8}\mathbb{I}$	♯Dof	$\mathbb{K} = 10^{-6}\mathbb{I}$	$\mathbb{K} = 10^{-8}\mathbb{I}$	♯Dof	$\mathbb{K} = 10^{-6}\mathbb{I}$	$\mathbb{K} = 10^{-8}\mathbb{I}$
232	3.8999e−16	3.1372e−15	152	2.4797e−16	2.7610e−15	405	9.1794e−16	7.0524e−16
880	8.4294e−16	6.4566e−15	560	5.1633e−16	5.5207e−15	1533	1.6588e−15	1.4514e−15
3424	1.5621e−15	1.2854e−14	2144	1.4743e−15	1.0995e−14	6089	3.2403e−15	3.2821e−15

6.4. Example 4

In this test, our method is applied to filtration problem [11,52]. The computational domain is concentric quarter circular divided into the free fluid and the porous medium domains as shown in Fig. 5(a), where the radii are $r_1 = 1$, $r_2 = 2$ and $r_3 = 3$. The inflow profile $\boldsymbol{u}_s = (-\frac{x}{30}, -\frac{y}{30})$ is imposed on $\Gamma_{s,1}$, $\boldsymbol{u}_s = \boldsymbol{0}$ is imposed on $\Gamma_{s,2}$ and $\Gamma_{s,3}$. We also impose zero Dirichlet condition on $\Gamma_{d,1}$ and slip condition $\boldsymbol{u}_d = \boldsymbol{0}$ on $\Gamma_{d,2}$ and $\Gamma_{d,3}$. Set $\boldsymbol{f} = \boldsymbol{0}$ in Ω_s and $g = 0$ in Ω_d. Choose the parameters as $\nu = 1$, $\alpha = \frac{0.1}{\sqrt{\beta}}$ (note that $\mathbb{K} = \beta\mathbb{I}$). We use quadrilateral mesh $\mathcal{T}_h$ with perturbed interior nodes as shown in Fig. 5(b). We first choose β to be 10^{-7} such that the permeability $\mathbb{K}$ in Ω_d is equal to

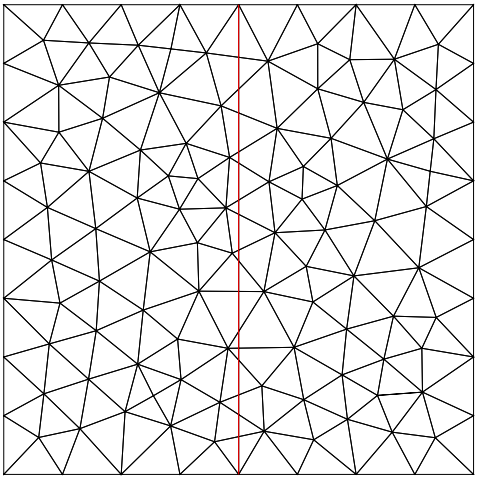

Fig. 4. Illustration of mesh $\mathcal{T}^8$ for Example 3. The vertical interface is colored in red. (For interpretation of the references to color in this figure legend, the reader is referred to the web version of this article.)

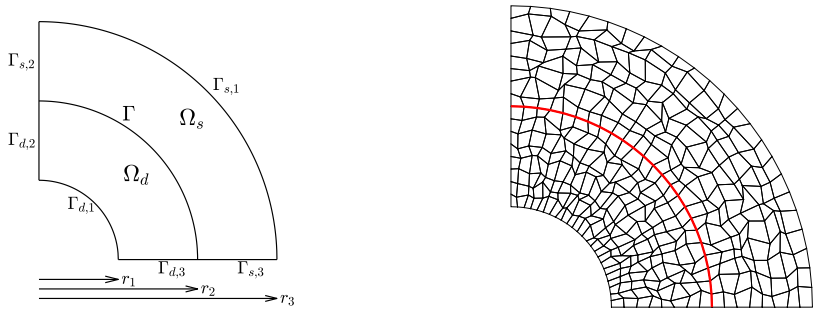

Fig. 5. (a): Computational domain for filtration problem; (b): illustration of mesh. The interface Γ is colored in red. (For interpretation of the references to color in this figure legend, the reader is referred to the web version of this article.)

$10^{-7}\mathbb{I}$. Considering the velocity $\boldsymbol{u}_h$ is not explicitly expressed, the $\boldsymbol{L}^2$ projection $\boldsymbol{\Pi}_h^o \boldsymbol{u}_h^{\text{div}}$ is plotted in Fig. 6(a), and the pressure p_h is presented in Fig. 6(b). Second, we choose a lower permeability, i.e., $\mathbb{K} = 10^{-12}\mathbb{I}$. The projection velocity $\boldsymbol{\Pi}_h^o \boldsymbol{u}_h^{\text{div}}$ and the pressure p_h are shown in Fig. 7, respectively. As we observe that the lower permeability results in a build up of the pressure. These results are consistent with those obtained in [11].

Another point we are interested in is the mass conservation. Let $\Gamma_{s,1,h} \subset \mathcal{F}_h$ be a partition of the inflow side $\Gamma_{s,1}$, and similarly, $\Gamma_{d,1,h}$ be a partition of the outflow side $\Gamma_{d,1}$. Since the inflow velocity $\boldsymbol{u}_s$ is provided, a simple computation gives the mass on the inflow side,

$$\Theta_{\text{in}} = \int_{\Gamma_{s,1}} \boldsymbol{u} \cdot \boldsymbol{n} \, \mathrm{d}s = \frac{3\pi}{20},$$

where $\boldsymbol{n}$ denotes the unit inward normal vector on $\Gamma_{s,1}$. After $\boldsymbol{u}_h$ is solved, the mass on the outflow side is computed by

$$\Theta_{\text{out}} = \int_{\Gamma_{d,1,h}} \boldsymbol{u}_h^{\text{div}} \cdot \boldsymbol{n} \, \mathrm{d}s,$$

where $\boldsymbol{n}$ denotes the unit outward normal vector on $\Gamma_{d,1,h}$. We also compute another type of mass on the inflow side as

$$\tilde{\Theta}_{\text{in}} = \int_{\Gamma_{s,1,h}} \boldsymbol{u} \cdot \boldsymbol{n} \, \mathrm{d}s.$$

Table 12
Mass difference between the inflow and outflow sides of the domain and the quantity δ for Example 4.

	$\mathbb{K} = 10^{-7}\mathbb{I}$			$\mathbb{K} = 10^{-12}\mathbb{I}$		
♯Dof	$\lvert\Theta_{\text{in}} - \Theta_{\text{out}}\rvert$	$\lvert\tilde{\Theta}_{\text{in}} - \Theta_{\text{out}}\rvert$	δ	$\lvert\Theta_{\text{in}} - \Theta_{\text{out}}\rvert$	$\lvert\tilde{\Theta}_{\text{in}} - \Theta_{\text{out}}\rvert$	δ
196	5.3646e−03	0	6.2986e−17	5.3646e−03	0	1.0538e−16
728	1.3446e−03	2.2204e−16	2.0268e−16	1.3446e−03	2.7756e−16	2.1411e−16
2800	3.3637e−04	1.0547e−15	4.2687e−16	3.3637e−04	8.8818e−16	2.9211e−15
10976	8.4105e−05	7.7716e−16	8.9465e−16	8.4105e−05	8.3217e−16	9.0375e−16
43456	2.1027e−05	5.5511e−16	1.7663e−15	2.1027e−05	4.9909e−16	1.8037e−15

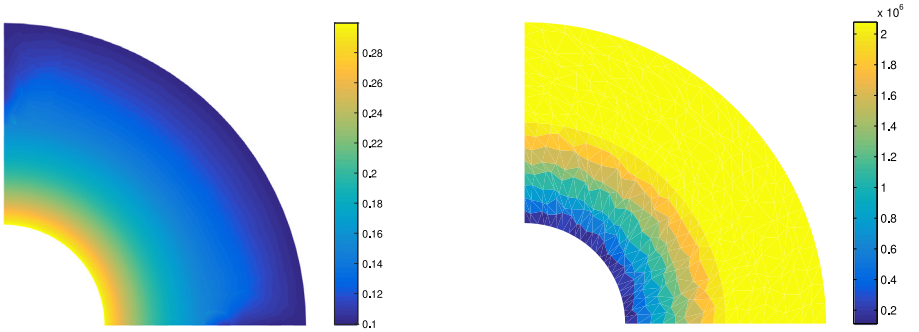

(a) (b)

Fig. 6. The Euclidean norm of $\boldsymbol{\Pi}_h^o \boldsymbol{u}_h^{\text{div}}$ (a) and the pressure p_h (b) with the permeability $\mathbb{K} = 10^{-7}\mathbb{I}$ in Example 4.

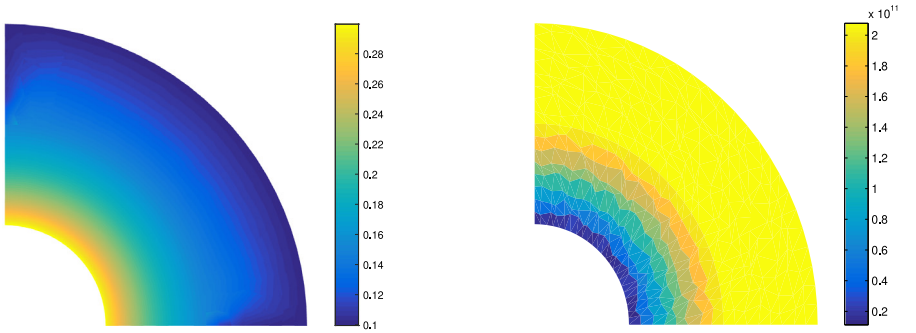

(a) (b)

Fig. 7. The Euclidean norm of $\boldsymbol{\Pi}_h^o \boldsymbol{u}_h^{\text{div}}$ (a) and the pressure p_h (b) with the permeability $\mathbb{K} = 10^{-12}\mathbb{I}$ in Example 4.

The mass differences $|\Theta_{\text{in}} - \Theta_{\text{out}}|$, $|\tilde{\Theta}_{\text{in}} - \Theta_{\text{out}}|$ and the quantity δ are reported in Table 12. On one hand, three numerical methods in [11] were employed for solving the Stokes–Darcy problem. And among the three, the DG–DG scheme of order two performs better and the corresponding rate of mass difference $|\Theta_{\text{in}} - \Theta_{\text{out}}|$ is $O(h^{3/2})$. From Table 12 we can observe a higher convergence rate $O(h^2)$ for all $\mathbb{K}$ compared with that of the DG–DG scheme of order two. On the other hand, we see that the mass difference $|\tilde{\Theta}_{\text{in}} - \Theta_{\text{out}}|$ is close to the computational accuracy. Note that the inflow side $\Gamma_{s,1}$ is a curve and its partition $\Gamma_{s,1,h}$ is a polygonal line. So that the partition $\mathcal{T}_h$ leads to mass loss to some extent and $|\Theta_{\text{in}} - \Theta_{\text{out}}|$ is larger than $|\tilde{\Theta}_{\text{in}} - \Theta_{\text{out}}|$ under the same d.o.f.

7. Conclusions

In this paper, we have presented a weak virtual element method on general meshes for the Stokes–Darcy problem. We use the $\boldsymbol{H}$(div) virtual element to discretize the velocity and discontinuous piecewise polynomials to approximate

the pressure. We also introduce a polynomial space on the element faces to approximate the tangential trace of the velocity in the Stokes equations. The velocity on the discrete level is exactly divergence free. Using the classical saddle point theory, we have proved the well-posedness of the discrete problem. Further, we derive an a priori error estimate that implies the velocity error is pressure-independent, which means our method is pressure-robust. A number of two-dimensional numerical experiments have shown the robustness of mass conservation and pressure with respect to the shape of grid and the permeability of the porous media. Our ongoing work is extending the method for solving the Navier–Stokes–Darcy problem. In the future, we will explore more general problems, such as time-dependent Stokes–Darcy problem and Stokes–Darcy/transport problem.

References

[1] G.S. Beavers, D.D. Joseph, Boundary conditions at a naturally permeable wall, J. Fluid Mech. 30 (1) (1967) 197–207.
[2] P.G. Saffman, On the boundary condition at the surface of a porous medium, Stud. Appl. Math. 50 (2) (1971) 93–101.
[3] Y. Cao, M. Gunzburger, X. He, X. Wang, Robin-Robin domain decomposition methods for the steady-state Stokes–Darcy system with the Beavers-Joseph interface condition, Numer. Math. 117 (4) (2011) 601–629.
[4] W. Chen, M. Gunzburger, F. Hua, X. Wang, A parallel Robin-Robin domain decomposition method for the Stokes–Darcy system, SIAM J. Numer. Anal. 49 (3) (2011) 1064–1084.
[5] M. Discacciati, A. Quarteroni, A. Valli, Robin-Robin domain decomposition methods for the Stokes–Darcy coupling, SIAM J. Numer. Anal. 45 (3) (2007) 1246–1268.
[6] X. He, J. Li, Y. Lin, J. Ming, A domain decomposition method for the steady-state Navier-Stokes–Darcy model with Beavers-Joseph interface condition, SIAM J. Sci. Comput. 37 (5) (2015) S264–S290.
[7] M. Mu, J. Xu, A two-grid method of a mixed Stokes–Darcy model for coupling fluid flow with porous media flow, SIAM J. Numer. Anal. 45 (5) (2007) 1801–1813.
[8] P. Chidyagwai, B. Rivière, On the solution of the coupled Navier-Stokes and Darcy equations, Comput. Methods Appl. Mech. Engrg. 198 (47–48) (2009) 3806–3820.
[9] B. Rivière, Analysis of a discontinuous finite element method for the coupled Stokes and Darcy problems, J. Sci. Comput. 22/23 (2005) 479–500.
[10] G. Wang, Y. He, R. Li, Discontinuous finite volume methods for the stationary Stokes–Darcy problem, Internat. J. Numer. Methods Engrg. 107 (5) (2016) 395–418.
[11] P. Chidyagwai, B. Rivière, Numerical modelling of coupled surface and subsurface flow systems, Adv. Water Resour. 33 (2010) 92–105.
[12] D. Vassilev, I. Yotov, Coupling Stokes–Darcy flow with transport, SIAM J. Sci. Comput. 31 (5) (2009) 3661–3684.
[13] F. Brezzi, M. Fortin, Mixed and Hybrid Finite Element Methods, Springer-Verlag, 1991, pp. 785–797.
[14] W.J. Layton, F. Schieweck, I. Yotov, Coupling fluid flow with porous media flow, SIAM J. Numer. Anal. 40 (6) (2002) 2195–2218 (2003).
[15] G.N. Gatica, S. Meddahi, R. Oyarzúa, A conforming mixed finite-element method for the coupling of fluid flow with porous media flow, IMA J. Numer. Anal. 29 (1) (2009) 86–108.
[16] G.N. Gatica, R. Oyarzúa, F.J. Sayas, Analysis of fully-mixed finite element methods for the Stokes–Darcy coupled problem, Math. Comp. 80 (276) (2011) 1911–1948.
[17] G.N. Gatica, R. Oyarzúa, F.J. Sayas, Convergence of a family of Galerkin discretizations for the Stokes–Darcy coupled problem, Numer. Methods Partial Differential Equations 27 (3) (2011) 721–748.
[18] G. Kanschat, B. Rivière, A strongly conservative finite element method for the coupling of Stokes and Darcy flow, J. Comput. Phys. 229 (17) (2010) 5933–5943.
[19] V. Girault, G. Kanschat, B. Rivière, Error analysis for a monolithic discretization of coupled Darcy and Stokes problems, J. Numer. Math. 22 (2) (2014) 109–142.
[20] B. Rivière, Discontinuous Galerkin methods for solving elliptic and parabolic equations: Theory and implementation, in: Frontiers in Applied Mathematics, vol. 35, Society for Industrial and Applied Mathematics (SIAM), Philadelphia, PA, 2008.
[21] C. Bernardi, T.C. Rebollo, F. Hecht, Z. Mghazli, Mortar finite element discretization of a model coupling Darcy and Stokes equations, M2AN Math. Model. Numer. Anal. 42 (3) (2008) 375–410.
[22] T. Karper, K.A. Mardal, R. Winther, Unified finite element discretizations of coupled Darcy-Stokes flow, Numer. Methods Partial Differential Equations 25 (2) (2009) 311–326.
[23] A. Márquez, S. Meddahi, F.J. Sayas, Strong coupling of finite element methods for the Stokes–Darcy problem, IMA J. Numer. Anal. 35 (2) (2015) 969–988.
[24] A. Márquez, S. Meddahi, F.J. Sayas, A decoupled preconditioning technique for a mixed Stokes–Darcy model, J. Sci. Comput. 57 (1) (2013) 174–192.
[25] L. Beirão da Veiga, F. Brezzi, A. Cangiani, G. Manzini, L.D. Marini, A. Russo, Basic principles of virtual element methods, Math. Models Methods Appl. Sci. 23 (1) (2013) 199–214.
[26] L. Beirão da Veiga, F. Brezzi, L.D. Marini, A. Russo, Virtual element method for general second-order elliptic problems on polygonal meshes, Math. Models Methods Appl. Sci. 26 (4) (2016) 729–750.
[27] L. Beirão da Veiga, F. Brezzi, L.D. Marini, A. Russo, The hitchhiker's guide to the virtual element method, Math. Models Methods Appl. Sci. 24 (8) (2014) 1541–1573.
[28] F. Brezzi, L.D. Marini, Virtual element methods for plate bending problems, Comput. Methods Appl. Mech. Engrg. 253 (2013) 455–462.

[29] L. Chen, H. Wei, M. Wen, An interface-fitted mesh generator and virtual element methods for elliptic interface problems, J. Comput. Phys. 334 (2017) 327–348.
[30] J. Wang, X. Ye, A weak Galerkin finite element method for second-order elliptic problems, J. Comput. Appl. Math. 241 (2013) 103–115.
[31] L. Mu, J. Wang, X. Ye, Weak Galerkin finite element methods on polytopal meshes, Int. J. Numer. Anal. Model. 12 (1) (2015) 31–53.
[32] J. Wang, X. Ye, A weak Galerkin mixed finite element method for second order elliptic problems, Math. Comp. 83 (289) (2014) 2101–2126.
[33] K. Lipnikov, G. Manzini, M. Shashkov, Mimetic finite difference method, J. Comput. Phys. 257 (part B) (2014) 1163–1227.
[34] L. Beirão da Veiga, V. Gyrya, K. Lipnikov, G. Manzini, Mimetic finite difference method for the Stokes problem on polygonal meshes, J. Comput. Phys. 228 (19) (2009) 7215–7232.
[35] A. Cangiani, G. Manzini, A. Russo, Convergence analysis of the mimetic finite difference method for elliptic problems, SIAM J. Numer. Anal. 47 (4) (2009) 2612–2637.
[36] D.A. Di Pietro, A. Ern, A hybrid high-order locking-free method for linear elasticity on general meshes, Comput. Methods Appl. Mech. Engrg. 283 (2015) 1–21.
[37] D.A. Di Pietro, S. Krell, A hybrid high-order method for the steady incompressible Navier-Stokes problem, J. Sci. Comput. (2) (2017) 1–29.
[38] B. Cockburn, J. Gopalakrishnan, R. Lazarov, Unified hybridization of discontinuous Galerkin, mixed, and continuous Galerkin methods for second order elliptic problems, SIAM J. Numer. Anal. 47 (2) (2009) 1319–1365.
[39] B. Cockburn, J. Gopalakrishnan, The derivation of hybridizable discontinuous Galerkin methods for Stokes flow, SIAM J. Numer. Anal. 47 (2) (2009) 1092–1125.
[40] Y. Jeon, E.J. Park, A hybrid discontinuous Galerkin method for elliptic problems, SIAM J. Numer. Anal. 48 (5) (2010) 1968–1983.
[41] W. Chen, F. Wang, Y. Wang, Weak Galerkin method for the coupled Darcy-Stokes flow, IMA J. Numer. Anal. 36 (2) (2016) 897–921.
[42] K. Lipnikov, D. Vassilev, I. Yotov, Discontinuous Galerkin and mimetic finite difference methods for coupled Stokes–Darcy flows on polygonal and polyhedral grids, Numer. Math. 126 (2) (2014) 321–360.
[43] G. Fu, C. Lehrenfeld, A strongly conservative hybrid DG/Mixed FEM for the coupling of Stokes and Darcy flow, J. Sci. Comput. (2018), http://dx.doi.org/10.1007/s10915-018-0691-0. Published online.
[44] L. Chen, F. Wang, A divergence free weak virtual element method for the Stokes problem on polytopal meshes, J. Sci. Comput. http://dx.doi.org/10.1007/s10915-018-0796-5.
[45] F. Brezzi, R.S. Falk, L.D. Marini, Basic principles of mixed virtual element methods, ESAIM Math. Model. Numer. Anal. 48 (4) (2014) 1227–1240.
[46] L. Beirão da Veiga, F. Brezzi, L.D. Marini, A. Russo, $H(\mathrm{div})$ and $H(\mathbf{curl})$-conforming virtual element methods, Numer. Math. 133 (2) (2016) 303–332.
[47] S.C. Brenner, L.Y. Sung, Virtual element methods on meshes with small edges or faces, Math. Models Methods Appl. Sci. 28 (7) (2018) 1291–1336.
[48] L. Chen, J. Huang, Some error analysis on virtual element methods, Calcolo 55 (1) (2018) Art. 5, 23.
[49] L. Beirão da Veiga, D. Mora, G. Rivera, R. Rodríguez, A virtual element method for the acoustic vibration problem, Numer. Math. 136 (3) (2017) 725–763.
[50] L. Chen, *i*FEM: An Integrated Finite Element Methods Package in MATLAB, Technical Report. University of California at Irvine. (2008).
[51] C. Talischi, G.H. Paulino, A. Pereira, I.F.M. Menezes, `PolyMesher`: A general-purpose mesh generator for polygonal elements written in Matlab, Struct. Multidiscip. Optim. 45 (3) (2012) 309–328.
[52] N.S. Hanspal, V. Nassehi, A. Kulkarni, Numerical analysis of coupled Stokes/Darcy flows in industrial filtrations, Transp. Porous Media 64 (1) (2006) 73–101.